Dynamic performance and control of Carnot battery-based combined cooling, heating and power systems with cascaded latent thermal energy stores

This is the PREPRINT version of this article. The final, published version of the article can be found at: https://doi.org/10.1016/j.apenergy.2025.127286

Jiaxing Huang[a], Yao Zhao[a,b,*], Jian Song[c,d], Jinwei Chen[a], Kai Wang[e], Zhenghua Rao[f], Christos N. Markides[d]

[a] *College of Smart Energy, Shanghai Jiao Tong University, Shanghai 200240, China*

[b] *Shanghai Non-carbon Energy Conversion and Utilization Institute, Shanghai Jiao Tong University, Shanghai 200240, China*

[c] *Birmingham Centre for Energy Storage & School of Chemical Engineering, University of Birmingham, Birmingham B15 2TT, UK*

[d] *Clean Energy Processes (CEP) Laboratory, Department of Chemical Engineering, Imperial College London, London SW7 2AZ, UK*

[e] *Institute of Refrigeration and Cryogenics & Key Laboratory of Refrigeration and Cryogenic Technology of Zhejiang Province, Zhejiang University, Hangzhou 310027, China*

[f] *School of Energy Science and Engineering, Central South University, Changsha 410083, China*

Abstract

Carnot batteries (CBs) can be extended into combined cooling, heating and power (CCHP) systems thanks to their conversion characteristics. Given the significant time-varying nature of load demands, achieving flexible responsiveness is critical for practical applications. In this study, a dynamic simulation model is developed for a CB-based CCHP system incorporating cascaded latent hot and cold stores, and a temperature-adaptive control strategy is proposed to enable rapid and flexible delivery of electricity, alongside multi-grade heating and cooling. By comparing different control solutions, the transient power generation performance and dynamic characteristics of delivering single and multi-grade hot/cold energy are analysed. The adaptability of the control strategy under variable operating conditions is further assessed, including coupling effects between power outputs and the impact of load variations on fluctuation errors. The results show that the control strategy ensures stable delivery of single and multi-grade hot/cold energy, achieving a trigeneration energy efficiency of 95% and an exergy efficiency of 55% in CCHP mode. Under variable operating conditions, the electrical, heating and cooling outputs can effectively track load variations within 200 s. The system exhibits robust synergistic anti-disturbance capability: disturbances in any single power output (electrical, heating or cooling) do not induce significant fluctuations in the others. However, power fluctuation errors increase with deviations from the design load and are more pronounced for high-grade heating/cooling outputs. This work provides operational guidance for the developing control strategies and for implementing CB-based CCHP systems.

* Corresponding author: zhaoyao@sjtu.edu.cn

Keywords

Combined cooling, heating and power; Carnot battery; Cascaded latent heat and cold stores; Control strategy; Dynamic operation

Nomenclature

Abbreviations

CB	Carnot battery	PCM	phase change material
CCHP	combined cooling, heating, and power	PTES	pumped-thermal electricity/energy storage
CLCS	cascaded latent cold store	RTE	roundtrip efficiency
CLHS	cascaded latent heat store	TES	thermal energy storage
CLHCS	cascaded latent heat and cold store	TEE	trigeneration energy efficiency
EXE	exergy efficiency	WF	working fluid

Greek symbols

α	liquid fraction	ρ	density (kg/m^3)
μ	dynamic viscosity (Pa·s)		

Symbols

A	heat transfer area, m^2	Nu	Nusselt number
c_p	specific heat capacity, J/(kg·K)	P	pressure, Pa
$\dot{E}x$	exergy transfer rate, W	Pr	Prandtl number
f	friction factor	$\dot{Q}$	heat transfer rate, W
H	enthalpy, J	r	tube radius, m
h	convective heat transfer coefficient, W/(m^2·K)	Re	Reynolds number
k	thermal conductivity, W/(m·K)	T	temperature, K
L	length of store, m	t	time, s
$\dot{m}$	mass flow rate, kg/s	v	bulk flow speed, m/s
N	total stage number	W	width, m
n	tube number	Δh	specific latent heat, J/kg

Superscripts and subscripts

c	charging	m	melting
d	discharging	o	outer
f	fluid	out	outlet
lat	latent enthalpy	ref	reference point
i	inner	sens	sensible enthalpy
in	inlet		

1. Introduction

To achieve carbon neutrality, renewable energy sources, exemplified by solar and wind power, are rapidly displacing traditional fossil fuels as the dominant contributors to global energy supply. According to statistical data from the International Renewable Energy Agency, worldwide renewable energy installed capacity surpassed 3.8 TW by 2023 [1]. Nevertheless, the inherent intermittency and volatility of these renewable sources present challenges in aligning with the continuously stabilised energy demand [2]. Against this backdrop, grid-scale energy storage technologies have emerged as an effective way to address the mismatch between renewable energy generation and consumption across time and space [3].

Among currently commercialised energy storage solutions, pumped hydro and compressed air storage systems exhibit relatively high technological maturity; however, their large-scale deployment is constrained by specific geographical requirements and high infrastructure costs [4-6]. While lithium-ion battery storage demonstrates second-level response capabilities, it suffers from inherent limitations including short cycle life and high large-scale costs [7]. In contrast, the emerging Carnot battery (CB) technology, distinguished by its geographical adaptability, long lifespan and cost-effectiveness, is rapidly becoming a research focus within the field of large-scale energy storage [8-10].

The operational principle of CB is based on the interconversion, storage and subsequent utilisation of electrical and thermal energy via integrated heat pump and heat engine cycles [11]. Notably, given the inherent dynamic variability in both renewable energy and user demand, the investigation of system dynamic characteristics and the development of adaptive control strategies have become the keys to addressing operational challenges and enabling large-scale deployment [12, 13].

Several studies concerning the dynamic characteristics and control strategies of CB systems have been reported in the literature, particularly those based on Joule–Brayton and organic Rankine cycle (ORC) configurations. Yang et al. [14, 15] developed a dynamic model of a Joule–Brayton cycle CB system employing liquid-based heat and cold stores, analysing the impact of power input disturbances and user-side load fluctuations on the system's dynamic performance. It was found that a 7% reduction in power input resulted in an exergy loss of 6.7% in the molten salt tanks. The study further revealed that both rotational speed and working fluid mass flow rate exhibited a positive correlation with power input during charging, and a negative correlation with load during discharging. Furthermore, under an inventory control strategy, the temperatures at each position of the system remained approximately constant. Frate et al. [16] evaluated the dynamic behaviour of a Joule–Brayton CB system with liquid-based heat and cold stores during last stages of the warm start-up and under a step increment of charge/discharge load, and they found that inventory control was essential for achieving steady-state design operation, while enabling rapid load adjustments with power input/output stabilisation achieved within approximately 20 s. Lu et al. [17] investigated the influence of rotational speed ramp rate and initial pressure on the start-up performance of such systems, and the analysis indicated that an optimal start-up can be achieved with a speed ramp rate of 100 rpm/s alongside initial pressures of 4.5 MPa during charging and 5 MPa during discharging. Subsequently, Shi et al. [18] proposed several variable load modes for such CB system, revealing a positive correlation between rotational speed

fluctuation rate and load adjustment range. They recommended that different variable load strategies should be selected based on rotor stability and the actual requirements of load regulation. An et al. [19] further developed a multi-physics dynamic system model, identifying that thermal inertia within liquid-based heat and cold stores induced an approximate 150 s system response delay. In addition, McTigue et al. [20] investigated the effect of ambient temperature on the temperature stability of liquid-based tanks, finding that under ambient temperature deviations of ±50 ℃, dynamic adjustment of the working fluid flow rate could effectively maintain the temperature stability of the tanks.

Beyond liquid-based heat and cold stores, Frate et al. [21] also assessed the off-design and part-load operational performance of a packed-bed Joule–Brayton CB configuration, examining the impact of packed-bed transient behaviour on turbine operation. The results revealed that the packed-bed temperature variations constrained the efficiency of the discharging cycle, thereby diminishing the system's roundtrip efficiency to less than 50%. Furthermore, Cascetta et al. [22] integrated a packed-bed Joule–Brayton CB with a concentrated solar power facility and analysed the operational performance of the coupled configuration. The results demonstrated that the system could operate stably by controlling the rotational speed of the compressor under varying solar radiation conditions, achieving a roundtrip efficiency of 54%.

Turning to ORC-based CB systems, Tosun et al. [23] analysed the dynamic performance of a solar PV-coupled ORC-CB configuration, taking into account the fluctuations in ambient temperature and irradiation rate throughout the day. They found that the coefficient of performance (COP) of the heat pump system varied between 2.3 and 4.5, while the thermal storage temperature fluctuated within the range of 94 to 100 ℃, under transient operating conditions. Similarly, Wang et al. [24] investigated the dynamic performance of a solar PV-coupled ORC-CB system over four representative days. They found that compressor power and system mass flow rate exhibited the most pronounced variations between 11:00 and 15:00 on the winter solstice, while the highest roundtrip efficiency, reaching 74%, was observed during the spring and autumn equinoxes.

The aforementioned studies have primarily focused on the charge-discharge functionality of CB. In fact, the fundamental thermoelectrical energy conversion principles enable these systems to be extended into combined cooling, heating and power (CCHP) systems [25, 26]. Furthermore, the integration of cascaded latent heat and cold stores (CLHCSs) can significantly enhance the grade diversity of the output thermal energy vectors, enabling delivery of electricity alongside thermal energy (for heating and/or cooling) at various grades [27-29].

However, despite recent advances in CB-based CCHP systems with CLHCSs, the dynamic interactions among electricity and multi-grade thermal energy remain inadequately understood, particularly under variable operating conditions. Existing studies have largely focused on steady-state performance or isolated subsystems, lacking comprehensive models that capture the coupled dynamics of such integrated systems. Furthermore, no established control strategies currently exist that can effectively coordinate multi-energy flows with both high responsiveness and stability under fluctuating loads or abrupt demand changes. This gap in knowledge restricts accurate real-time performance prediction and prevents the practical implementation of flexible, demand-responsive generation of electricity alongside multi-grade thermal energy.

In this paper, a dynamic simulation model of a CB-based CCHP system with CLHCSs is established,

accompanied by the development of a temperature-adaptive control strategy aimed at enabling rapid and flexible delivery of electricity alongside multi-grade thermal energy for both heating and cooling. The influence of different control solutions on the instantaneous power generation performance is compared, and the transient response characteristics under both single-grade and multi-grade heating/cooling outputs are analysed. Furthermore, the applicability and feasibility of the proposed control strategy under variable operating conditions are explored, with an examination of the interrelations among electrical, heating and cooling power, as well as the impact of load levels on power fluctuation errors.

The key contributions of this work are: (1) a comprehensive characterisation of transient multi-energy interactions within CB-based CCHP systems with CLHCSs, (2) a control methodology enabling rapid response to load variations while preserving operational stability. These advances establish a foundation for more accurate prediction of system behaviour and open new pathways for demand-responsive, reliable multi-energy management.

2. Modelling methodology

2.1. System layout and description

A schematic diagram of a Joule-Brayton cycle CB-based CCHP system is shown in Figure 1. The configuration incorporates co-axially arranged compressor-expander units, cascaded latent heat stores (CLHSs), cascaded latent cold stores (CLCSs), and heat exchangers.

A schematic of the shell-and-tube type CLHCS unit is shown in Figure 2. Both CLHSs and CLCSs consist of five distinct stages, with PCMs arranged sequentially according to melting temperature, ascending from Stage 1 to Stage 5 in the CLHSs, and descending from Stage 1 to Stage 5 in the CLCSs, as shown in Figure 2(a) and Figure 2(b). Each individual hot/cold store incorporates multiple identical basic storage elements featuring a square cross-section, as shown in Figure 2(c) and Figure 2(d). The working fluid (WF) flows inside the circular tubes, transferring thermal energy to or from the PCMs externally.

During charging, as shown in Figure 1(a), electrical input from renewable sources or grid surplus drives the compressor, elevating the WF to a state of high temperature and pressure. The WF then enters the CLHSs, transferring heat energy sequentially to the PCMs in successive stages. Following this, the WF expands to a low-temperature state and enters the CLCSs, releasing cold energy stage by stage to the PCMs. To maintain operational efficiency, heat exchangers HX1 and HX2 dissipate residual waste cold and heat energy, respectively.

During discharging, as shown in Figure 1(b), the system delivers electricity alongside multi-grade thermal energy for heating and cooling, enabling operation in PES and CCHP modes. Specifically, in PES mode, the WF is cooled by absorbing cold energy from the CLCSs. Following compression to high pressure, the WF absorbs heat within the CLHSs before expanding in the expander to generate electricity. In CCHP mode, while the primary circuit generates electricity, an auxiliary WF stream enters targeted stages of the CLHSs and CLCSs to extract (hot/cold) thermal energy at the required temperatures for end-user delivery.

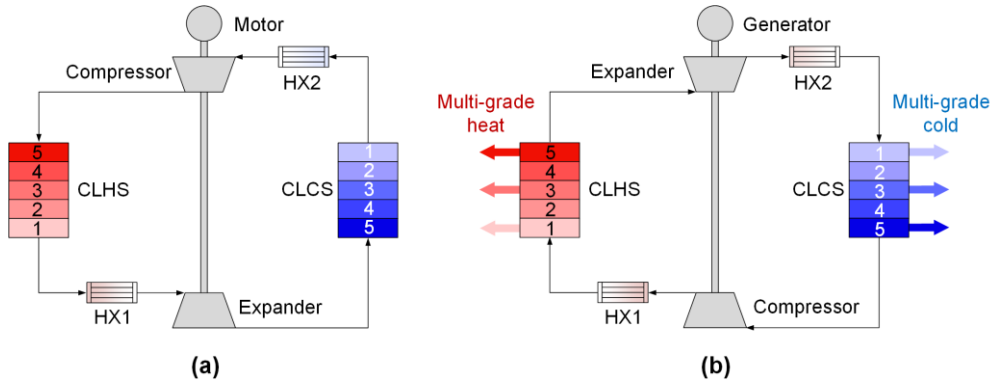


Figure 1. Schematic diagram of a CB-based CCHP system: (a) charging process, and (b) discharging process.

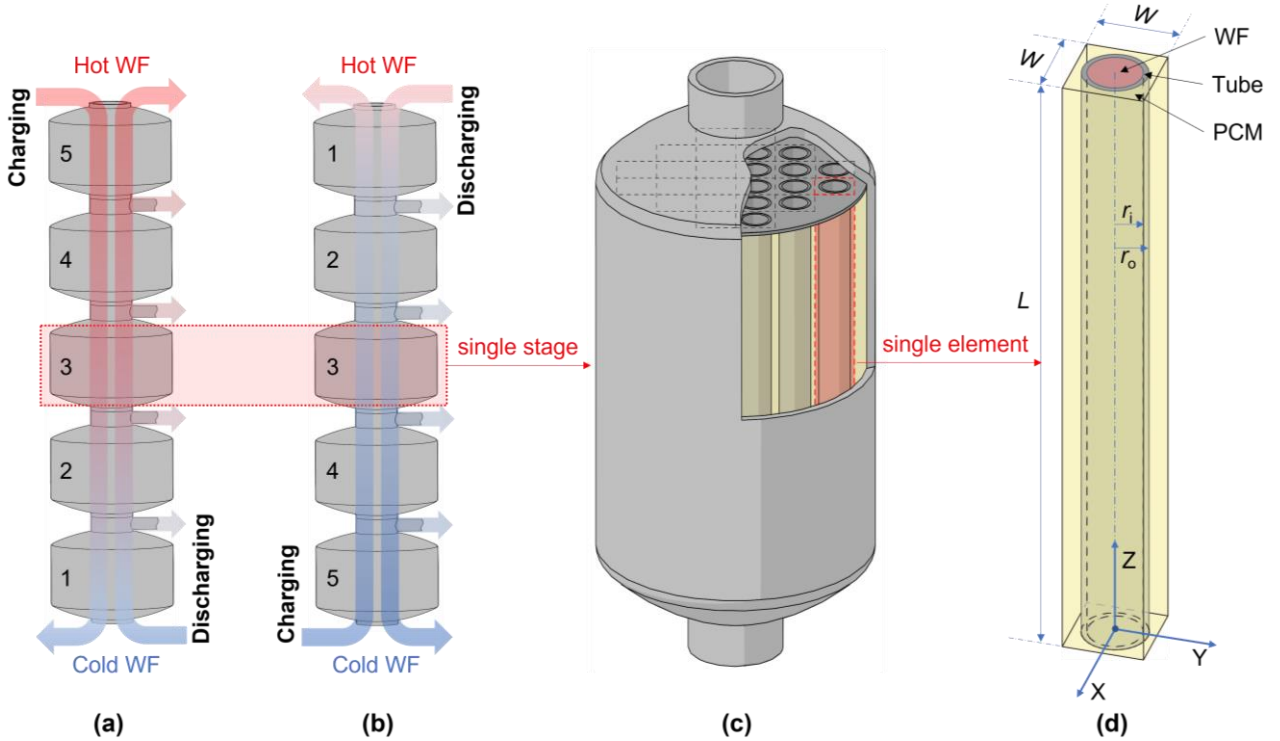


Figure 2. Schematic diagram of: (a) cascaded latent heat stores, (b) cascaded latent cold stores, (c) single hot/cold store, and (d) single storage element.

2.2. System model

The system model is established to capture the coupled thermodynamic and dynamic behaviours of the CB-based CCHP system.

2.2.1 Turbomachinery

The power consumed by the compressor is determined by:

$$\dot{w}_c = \dot{m}_f \left(h_{f,c,out} - h_{f,c,in} \right) \tag{1}$$

where $\dot{m}_f$ is the WF mass flow rate, and $h_{f,c,out}$ and $h_{f,c,in}$ represent the specific enthalpy at compressor outlet/inlet, respectively.

The expander output power is given by:

$$\dot{w}_{\mathrm{e}} = \dot{m}_{\mathrm{f}} \left(h_{\mathrm{f,e,in}} - h_{\mathrm{f,e,out}} \right) \tag{2}$$

where $h_{\mathrm{f,e,in}}$ and $h_{\mathrm{f,e,out}}$ are the specific enthalpy at expander inlet/outlet, respectively.

The temperature ratio π_{c} and pressure ratio β_{c} of the compressor are determined by:

$$\pi_{\mathrm{c}} = \frac{\beta_{\mathrm{c}}^{\frac{\gamma-1}{\gamma}} - 1}{\eta_{\mathrm{c}}} + 1 \tag{3}$$

where η_{c} is the entropic efficiency of the compressor, and γ is the specific heat ratio.

The temperature ratio π_{e} and pressure expansion ratio β_{e} of the expander are determined by:

$$\pi_{\mathrm{e}} = \frac{\beta_{\mathrm{e}}^{\frac{\gamma-1}{\gamma}} - 1}{\eta_{\mathrm{e}}} + 1 \tag{4}$$

where η_{e} is the isentropic efficiency of the expander.

The actual compression ratio and the compression efficiency of the compressor under off-design conditions are determined by [30, 31]:

$$\beta_{\mathrm{c}} = \beta_{\mathrm{c},0} \left(c_1 \dot{n} \dot{G}^2 + c_2 \dot{n} \dot{G} + c_3 \dot{n} \right) \tag{5}$$

$$\eta_{\mathrm{c}} = \eta_{\mathrm{c},0} \left[1 - c_4 \left(1 - \dot{n} \right)^2 \right] \frac{\dot{n}}{\dot{G}} \left(2 - \frac{\dot{n}}{\dot{G}} \right) \tag{6}$$

where $\dot{G}$ and $\dot{n}$ are the reduced flow rate and the reduced rotational speed, respectively. c_1, c_2, c_3, and c_4 are characteristic curve coefficients, and the subscript 0 denotes design conditions.

$$\dot{G} = \frac{\dot{m}\sqrt{T_{\mathrm{in}}} \,/\, p_{\mathrm{in}}}{\left(\dot{m}\sqrt{T_{\mathrm{in}}} \,/\, p_{\mathrm{in}} \right)_0} \tag{7}$$

$$\dot{n} = \frac{n / \sqrt{T_{\mathrm{in}}}}{\left(n / \sqrt{T_{\mathrm{in}}} \right)_0} \tag{8}$$

The expander performance parameters similarly vary with inlet conditions, and the off-design behaviour is characterised by [14, 30]:

$$\eta_{\mathrm{e}} = \eta_{\mathrm{e},0} \left[1 - 0.3 \left(1 - \dot{n} \right)^2 \right] \frac{\dot{n}}{\dot{G}} \left(2 - \frac{\dot{n}}{\dot{G}} \right) \tag{9}$$

$$\frac{\dot{m}_{\mathrm{e}}}{\dot{m}_{\mathrm{e},0}} = \sqrt{1.4 - 0.4 \frac{n}{n_0}} \sqrt{\frac{T_{\mathrm{e,0,in}}}{T_{\mathrm{e,in}}}} \sqrt{\frac{\beta_{\mathrm{e}}^2 - 1}{\beta_{\mathrm{e},0}^2 - 1}} \tag{10}$$

2.2.2 Cascaded latent heat and cold stores

The energy conservation equation for the WF in the tubes is expressed as [32-34]:

$$\rho_{\mathrm{f}} c_{\mathrm{p,f}} A \frac{\partial T_{\mathrm{f}}}{\partial t} = -\rho_{\mathrm{f}} c_{\mathrm{p,f}} A v_{\mathrm{f}} \frac{\partial T_{\mathrm{f}}}{\partial z} - \dot{Q}_{\mathrm{wall}} \tag{11}$$

where ρ_{f} denotes the WF density, $c_{\mathrm{p,f}}$ is the specific heat capacity, A is the cross-sectional area of the WF bulk (tube), T_{f} is the WF bulk temperature, $\dot{Q}_{\mathrm{wall}}$ is the heat transfer rate between the WF and the tube wall, and v_{f} is the WF bulk flow velocity, which can be calculated from:

$$v_{\mathrm{f}} = \frac{\dot{m}_{\mathrm{f}}}{n_{\mathrm{tube}} \rho_{\mathrm{f}} \pi r_{\mathrm{i}}^2} \tag{12}$$

where $\dot{m}_{\mathrm{f}}$ is the WF mass flow rate, n_{tube} is the number of tubes, and r_{i} is the inner tube radius.

In addition, $\dot{Q}_{\mathrm{wall}}$ can be calculated from [35]:

$$\dot{Q}_{\mathrm{wall}} = h_{\mathrm{f}} \left(T_{\mathrm{f}} - T_{\mathrm{tube}} \right) 2\pi r_{\mathrm{i}} \tag{13}$$

where T_{tube} is the temperature of the tube wall, and h_{f} is the convective heat transfer coefficient, given by [36]:

$$h_{\mathrm{f}} = \frac{k_{\mathrm{f}}}{2r_{\mathrm{i}}} Nu \tag{14}$$

with k_{f} the WF thermal conductivity, and the Nusselt number Nu is calculated as [36]:

$$Nu = \begin{cases} 3.66 & \left(Re \le 2200\right) \\ \dfrac{(f/8)\left(Re - 1000\right) Pr}{1 + 12.7 (f/8)^{1/2} \left(Pr^{2/3} - 1\right)} & \left(2200 < Re \le 5 \times 10^6\right) \\ 0.23 \left(Re^{0.8} Pr^{0.4}\right) & \left(Re > 5 \times 10^6\right) \end{cases} \tag{15}$$

where Pr is the Prandtl number, and f and Re are the friction factor and Reynolds number [36]:

$$f = \begin{cases} \dfrac{64}{Re} & Re \le 2200 \\ \dfrac{1}{(0.79 \ln Re - 1.64)^2} & Re > 2200 \end{cases} \tag{16}$$

$$Re = \frac{2 \rho_{\mathrm{f}} v_{\mathrm{f}} r_{\mathrm{i}}}{\mu_{\mathrm{f}}} \tag{17}$$

with μ_{f} the dynamic viscosity of the WF.

The pressure drop Δp in CLHS/CLCS units is calculated as [36]:

$$\Delta p = \frac{f \rho_{\mathrm{f}} v_{\mathrm{f}}^2 L_{\mathrm{tot}}}{4 r_{\mathrm{i}}} \tag{18}$$

Energy conservation for the tube can be expressed by:

$$\rho_{\text{tube}} c_{\text{p,tube}} \frac{\partial T_{\text{tube}}}{\partial t} = k_{\text{tube}} \left(\frac{\partial^2 T_{\text{tube}}}{\partial x^2} + \frac{\partial^2 T_{\text{tube}}}{\partial y^2} + \frac{\partial^2 T_{\text{tube}}}{\partial z^2} \right) \tag{19}$$

where ρ_{tube} denotes the density of the tube's material, $c_{\text{p,tube}}$ the specific heat capacity of the material, and k_{tube} the thermal conductivity of the material.

For shell-and-tube storage unit configurations, when the specific geometric parameter $S = (R^2\text{-}r^2)/(2rL)$ (where R is the outer radius of the PCM, r the tube radius, and L the tube length) is less than 0.005, and the Rayleigh number is below 8×10^5, the effect of natural convection within the PCM can be neglected [34]. In the present study, the adopted value of S is 0.001 and the Rayleigh number is 2.6×10^5, satisfying the criteria for neglecting natural convection effects.

The energy conservation for the PCM is governed by [32, 34]:

$$\rho_{\text{PCM}} \frac{\partial H_{\text{PCM}}}{\partial t} = k_{\text{PCM}} \left(\frac{\partial^2 T_{\text{PCM}}}{\partial x^2} + \frac{\partial^2 T_{\text{PCM}}}{\partial y^2} + \frac{\partial^2 T_{\text{PCM}}}{\partial z^2} \right) \tag{20}$$

where ρ_{PCM} and k_{PCM} represent PCM density and thermal conductivity, respectively, T_{PCM} denotes local temperature, and H_{PCM} is the PCM enthalpy, which is composed of sensible enthalpy h_{sensible} and latent enthalpy h_{latent}:

$$H_{\text{PCM}} = H_{\text{sensible}} + H_{\text{latent}} \tag{21}$$

$$H_{\text{sensible}} = H_{\text{ref}} + \int_{T_{\text{ref}}}^{T_{\text{PCM}}} c_{\text{p, PCM}} dT_{\text{PCM}}, \; H_{\text{latent}} = \Delta h \alpha \tag{22}$$

where H_{ref} denotes the reference enthalpy, $c_{\text{p,PCM}}$ is the PCM specific heat capacity, Δh signifies the latent heat of fusion, and α represents the liquid fraction, defined as:

$$\alpha = \begin{cases} 0 & T < T_{\text{solidus}} \\ (T - T_{\text{solidus}}) / (T_{\text{liquidus}} - T_{\text{solidus}}) & T_{\text{solidus}} \le T \le T_{\text{liquidus}} \\ 1 & T > T_{\text{liquidus}} \end{cases} \tag{23}$$

2.2.3 Heat exchangers

The energy conservation equation applied to any heat exchanging component can be expressed by [37]:

$$\dot{m}_{\text{h}} c_{\text{p,h}} \left(T_{\text{h,in}} - T_{\text{h,out}} \right) - \dot{Q}_{\text{HX}} = M_{\text{h}} c_{\text{p,h}} \frac{\text{d}T_{\text{h,avg}}}{\text{d}t} \tag{24}$$

$$\dot{m}_{\text{c}} c_{\text{p,c}} \left(T_{\text{c,in}} - T_{\text{c,out}} \right) + \dot{Q}_{\text{HX}} = M_{\text{c}} c_{\text{p,c}} \frac{\text{d}T_{\text{c,avg}}}{\text{d}t} \tag{25}$$

where $c_{\text{p,h}}$ and $c_{\text{p,c}}$ denote the specific heat capacities of the hot-side and cold-side fluids, respectively; $T_{\text{h,in}}$, $T_{\text{h,out}}$, $T_{\text{c,in}}$ and $T_{\text{c,out}}$ represent the hot inlet, hot outlet, cold inlet, and cold outlet temperatures; M_{h} and M_{c} are the fluids masses in hot and cold sides, respectively; $T_{\text{h,avg}}$ and $T_{\text{c,avg}}$ signify the average temperatures of the

fluids in hot and cold sides, respectively; $\dot{Q}_{HX}$ is the heat transfer rate, and can be can be obtained by:

$$\dot{Q}_{HX} = U_{HX} A_{HX} \Delta T_m \tag{26}$$

where U_{HX} is the overall heat transfer coefficient, A_{HX} the heat transfer area of the heat exchanger, and ΔT_m the log-mean temperature difference.

2.2.4 Compressor and expander shafts

To capture the speed variations of the compressor and expander during rotation, the shaft model employs the angular momentum balance expressed as:

$$\frac{d\omega}{dt} = \frac{1}{J\omega}(P_m - \dot{w}_c + \dot{w}_e) \tag{27}$$

$$\frac{d\omega}{dt} = \frac{1}{J\omega}(\dot{w}_e - \dot{w}_c - P_g) \tag{28}$$

where ω denotes angular velocity, J represents the total moment of inertia, P_m is the motor input power, and P_g is the power load. Electrical conversion efficiency and mechanical losses are assumed to be negligible.

2.2.5 Performance indicators

The power-to-power roundtrip efficiency (*RTE*) is defined as:

$$RTE = \frac{E_{output}}{E_{input}} \tag{29}$$

where E_{output} and E_{input} represent the net output electric energy during discharging and net input electric energy during charging, respectively, which are calculated as:

$$E_{input} = (\dot{w}_c - \dot{w}_e) t_c \tag{30}$$

$$E_{output} = (\dot{w}_e - \dot{w}_c) t_d \tag{31}$$

where t_c and t_d represent the charging and discharging duration, respectively.

The trigeneration energy efficiency (*TEE*), based on the first law of thermodynamics, measures the CCHP system's overall energy utilisation:

$$TEE = \frac{E_{output} + Q_{heat} + Q_{cold}}{E_{input}} \tag{32}$$

where Q_{heat} and Q_{cold} are the net heating and cooling thermal energy outputs from the system, respectively.

Governing the second law of thermodynamics, the system's exergy efficiency (*EXE*) is defined as:

$$EXE = \frac{E_{\text{output}} + Ex_{\text{heat}} + Ex_{\text{cold}}}{E_{\text{input}}} \tag{33}$$

where Ex_{heat} and Ex_{cold} signify the output heat exergy and cold exergy delivered by the system, respectively.

2.3. Numerical methodology and model validation

Spatial discretisation is performed using the Galerkin finite element method, while the transient terms are discretised with an implicit backward difference formula (BDF). The resulting discrete nonlinear system is subsequently solved using a damped Newton method, integrated within the ODE15s solver for time advancement.

To ensure the reliability of the developed model, its predictions are compared with available experimental data under identical operating conditions. For the CLHCS unit, numerical predictions are compared with experimental results [38] under identical operating conditions. The latent heat storage unit has an outer diameter of 0.0258 m and a length of 1.0 m, with n-octadecane employed as the PCM. As shown in Figure 3(a), the temperatures at two locations within the PCM (Point 1 and Point 2), situated 0.002 m and 0.001 m from the HTF tube respectively, are compared. The simulated results exhibit close agreement with the experimental measurements, with relative deviations remaining within 2%.

Similarly, the heat exchanger model is validated against experimental results [39], as shown in Figure 3(b). To investigate its transient behaviour, temperature shocks are imposed at the hot inlet: a cold shock, with the inlet temperature decreasing from 783 K to 453 K within 5 s, and a hot shock, with the temperature rising from 453 K to 783 K over 120 s. The inlet temperature on the cold side is maintained constant at 378 K. During the simulation, the outlet temperatures of both the hot and cold sides exhibit periodic variations. In comparison with the experimental data, the model captures the response trend well, with deviations remaining below 3%.

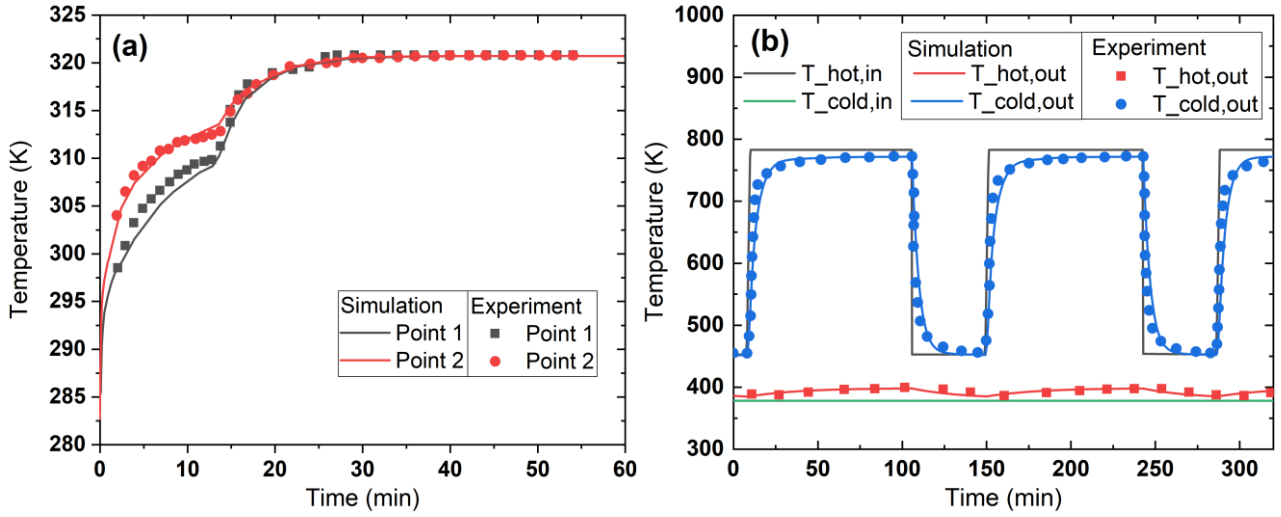


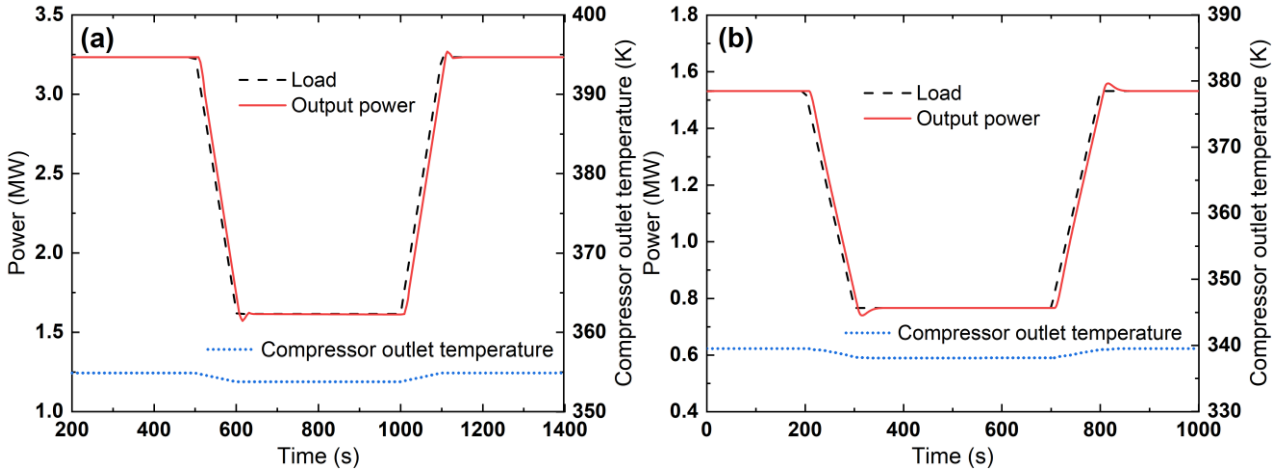
Figure 3. Verification of simulation results.

In addition, the performance of the turbomachinery components is compared with the reference [40]. At a pressure ratio of 4.3, the outlet temperatures and pressures of both the compressor and the expander are

compared under identical inlet conditions, as summarised in Table 1. The results demonstrate good agreement, with differences smaller than 0.5%. This turbomachinery model has also been employed in the literature [17, 41, 42]. Taken together, these close agreements demonstrate that the numerical model provides reliable predictions and is well suited for the present investigation.

Table 1. Comparison of the compressor and expander

	Component	Outlet temperature (K)	Outlet pressure (kPa)
Reference [40]	Compressor	860.7	106.5
	Expander	198.7	24.8
This model	Compressor	859.8	106.1
	Expander	199.5	24.7



2.4 Control strategy

During the discharge process, the temperature variations of the PCM within CLHCS lead to a progressive decrease in the WF temperature at each stage outlet. To achieve stable hot/cold energy output at a constant temperature, this study proposes a temperature-adaptive control strategy. The core principle of this strategy is the real-time adjustment of the WF mass flow rate at each stage. By optimally blending the outlet fluids from the cascaded units at varying temperatures, the actual outlet temperature decline at each stage can be compensated, thereby precisely maintaining the stability of the target output temperature.

Specifically, taking the CLHS as an example, during the heat discharge process, the WF flowing out of the high-level storage unit (higher storage temperature) is at a higher temperature, whereas the WF flowing out from the low-level unit (lower storage temperature) is at a relatively lower temperature, due to the inherent multi-level temperature distribution characteristic of the cascaded units. This strategy dynamically calculates and controls the WF mass flow rates flowing through the specific high-level unit and low-level units, and achieves a constant target output temperature by matching and mixing the higher-temperature WF with the lower-temperature WF.

However, the matching solution capable of satisfying the target temperature requirement is not unique; e.g., the highest-temperature stream may be paired with the lowest-temperature stream, or two streams with temperatures close to the target value may be matched instead. To ensure the cascade utilisation of thermal energy quality, the control strategy adopts a matching solution that minimises exergy loss within the hot/cold discharge process.

In this study, we employed a proportional-integral-derivative (PID) control algorithm:

$$u(t) = K_{\mathrm{p}} e(t) + K_{\mathrm{i}} \int_0^t e(t)\mathrm{d}t + K_{\mathrm{d}} \frac{\mathrm{d}e(t)}{\mathrm{d}t} \tag{34}$$

where $u(t)$ is the control signal, regulating the valve opening position to adjust the WF mass flow rate within the thermal storage unit. $e(t)$ is the error between the target temperature and the actual temperature. K_{p} is the proportionality factor, K_{i} is the integration factor, and K_{d} is the differentiation factor.

The specific control process is shown in Figure 4. First, the outlet temperatures $T_{\mathrm{out},i}$ from each stage of the CLHCS are assessed to identify potential energy supply stages, that is, the possible WF flow solutions capable of meeting the temperature requirement. For each candidate solution, the corresponding exergy loss rate is evaluated, and the solution with the minimum exergy loss is identified, thereby determining the optimal stages for energy supply to be activated through valve regulation. Next, a PID controller is employed to measure the deviation between the target and actual temperatures, and to compute the appropriate valve openings that adjust the working fluid mass flow rate within each stage of the CLHCS. This ensures that T_{mix} rapidly converges to and stabilises at T_{actual}.

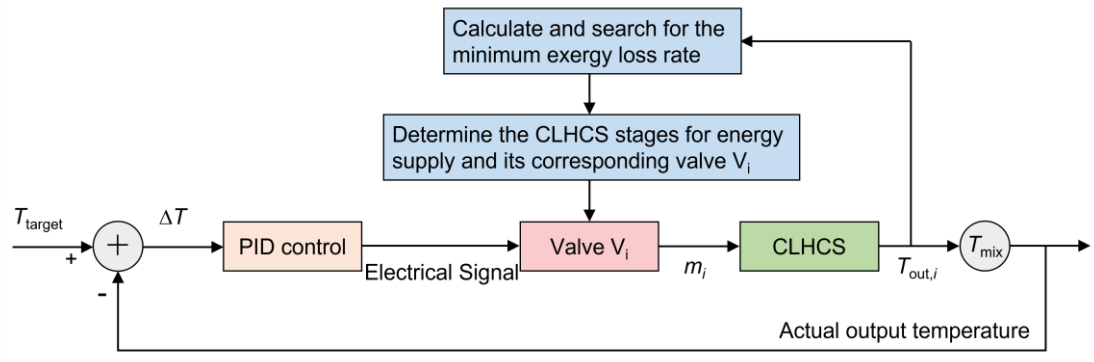


Figure 4. Schematic diagram of control strategy.

2.5 Parameter setting

Argon is selected as the WF for the CB system, consistent with prior studies demonstrating superior round-trip efficiency [43-45]. The detailed operating conditions and CLHCS design parameters are summarised in Table 2. To mitigate risks of structural compromise at temperature extremes, operational boundaries are constrained to 850 K (maximum) and 125 K (minimum). The isentropic efficiencies of the compressor and expander are set at 90% and 95%, respectively. For optimal *RTE*, pressure ratios are set to be 11.6 during charging and 8.0 during discharging under design conditions [25, 26].

The tubes within CLHCSs are 3/4-in. O.D., 16 BWG (Birmingham Wire Gage) type, commonly employed in

heat exchanger components [27]. Each basic PCM element has a width set to 1.5 times the tube diameter to optimise heat transfer effectiveness [46]. While the large stage length and small tube number in CLHCSs enhance heat transfer effectiveness, these features also increase system size, cost and cause significant pressure losses. Based on previous studies [26], the design parameters in Table 2 are selected to optimise thermodynamic performance while avoiding excessive physical size.

PCMs with melting points within this study's operational temperature range include organic compounds (e.g., lauric acid, paraffin wax, adipic acid) and inorganic salts such as KNO_3, $MgCl_2$-NaCl (52:48 wt%), Li_2CO_3-K_2CO_3 (35:65 wt%), etc. Some potentially feasible PCMs are selected for the case study, as shown in Table 3 [47-49].

Table 2. Operating conditions and CLHCS design parameters.

Conditions and parameters	**Unit**	**Value**
Ambient temperature, T_{am}	K	298
Argon mass flow rate for power, $\dot{m}_{f,p}$	kg/s	12.5
Argon mass flow rate for heating/cooling, $\dot{m}_{f,hc}$	kg/s	6.25
Charging-discharging duration, t_{cd}	s	21600
Maximum system operating temperature	K	850
Minimum system operating temperature	K	125
Compressor isentropic efficiency, η_c	%	90
Expander isentropic efficiency, η_e	%	95
Pressure ratio during charging, β_1	-	11.6
Pressure ratio during discharging, β_2	-	8.0
Tube outer & inner radius, r_o & r_i	m	9.5×10^{-3} & 7.85×10^{-3}
Thermal conductivity of tube material, k_{tube}	W/(m·K)	21.4
Width of the PCM element, W_{PCM}	m	2.86×10^{-2}
Tube number	-	2500
Stage length	m	10

Table 3. Thermophysical properties of selected PCMs [47-49].

	Stage	**Materials**	**Melting temperature [K]**	**Specific latent heat [kJ/kg]**	**Density [kg/m^3]**	**Thermal conductivity [W/(m·K)]**
CLHS	1	$LiNO_3$-KCl (58:42 wt%)	433	272	2196	0.9
	2	LiCl-LiOH (51:49 wt%)	535	485	1550	1.1
	3	Li_2CO_3-Na_2CO_3-K_2CO_3 (32:33:35 wt%)	661	388	2084	1.9
	4	Li_2CO_3-K_2CO_3 (47:53 wt%)	757	300	1850	0.6

	5	Al-Cu (67:33 wt%)	821	351	1110	80
CLCS	1	E-15	258	320	1060	0.5
	2	SP-50	223	200	1300	0.6
	3	E-90	183	90	786	0.2
	4	E-114	159	107	782	0.2
	5	Butane	136	80	735	0.2

3. Results and discussion

3.1. Design operating condition

Under design operating conditions, the CB-based CCHP system is designed to deliver electricity at stable power output, together with heat and "cold" energy at constant temperatures. Since electricity generation relies on the Joule-Brayton cycle, the stable operation of both the expander and compressor is critically important. Figure 5 shows the temporal evolution of the WF temperature at the outlets of each stage within the CLHS and CLCS when all system parameters are maintained at their design values. In both the CLHS and CLCS, the WF flows sequentially from Stage 1 to Stage 5, reaching its highest and lowest temperatures at the Stage 5 outlet, respectively. However, the WF temperature exiting the CLHS exhibits a gradual decrease over time, while that exiting the CLCS shows a gradual increase. If these thermally unstable flows were directly fed into the expander and compressor, respectively, these temperature variations would compromise operational stability and degrade efficiency. Therefore, to achieve stable output temperatures for hot/cold energy and maintain steady system operation, it is essential to implement the proposed temperature adaptive control strategy.

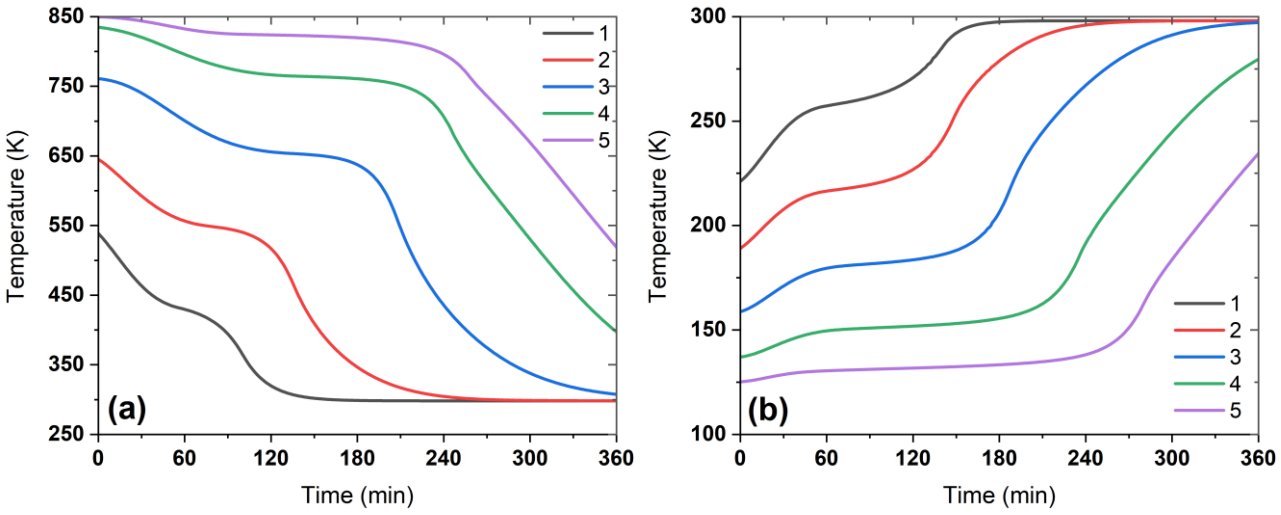


Figure 5. Temporal variation of WF temperature at the outlet of each stage in: (a) CLHS, and (b) CLCS, when the WF mass flow rate is the design value.

3.1.1 PES mode

To analyse the performance of the proposed control strategy, alternative solutions are also evaluated and compared alongside the exergy-loss-minimising solution, as shown in Figure 6. Among them, Solutions 1, 2, and 3 serve as counterpart solutions for comparison, while Solution 4 exhibits the exergy-loss-minimising solution. Solution 1 involves diverting the WF at the Stage 1 outlet, achieving the target temperature by mixing two WF streams with temperatures $T_{out,5}$ and $T_{out,5}$, respectively. Solution 2 diverts the WF at the Stage 2 outlet, blending the WF temperatures of the Stage 2 and Stage 5 outlets. Solution 3 implements diversion at the Stage 3 outlet. Solution 4 proceeds in two steps: Step 1, the WF is diverted at the Stage 3 outlet when $T_{out,4}$ is greater than the target temperature; otherwise, the Step 2 is executed, in which the WF is diverted at the Stage 4 outlet.

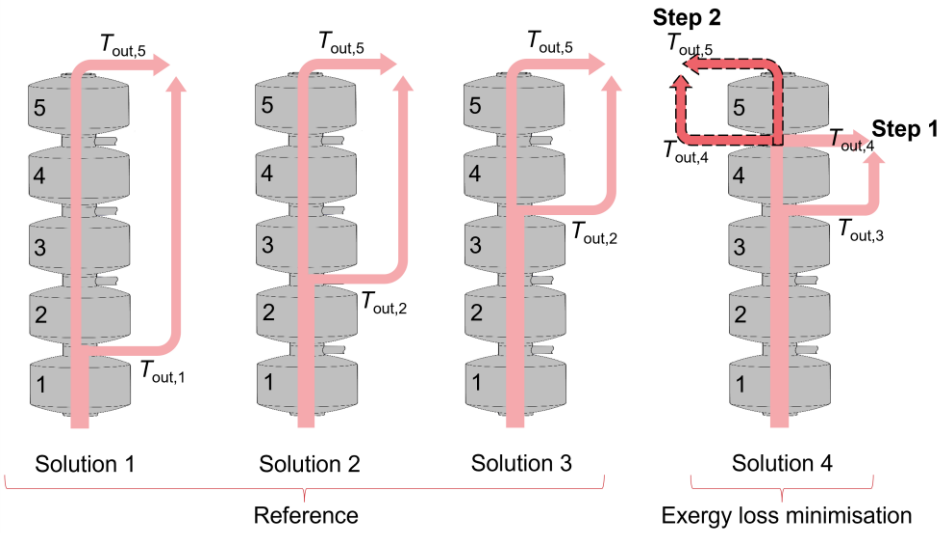


Figure 6. Schematic diagram of WF flow distribution for the four control solutions.

Figure 7 shows the actual output temperatures under the four control solutions. It can be seen that Solutions 1, 2 and 3 achieve stable temperature outputs for both the CLHS and CLCS, with deviations from the design values of 800 K and 140 K remaining within 0.2 K, demonstrating effective control performance. For Solution 4, the output temperatures of the CLHS and CLCS are generally stable; however, fluctuations of 2 K occur at 73 min and 17 min, reaching 802 K and 138 K, respectively. These fluctuations result from changes in the heating and cooling stages—specifically, the transition from Step 1 to Step 2, as shown in Figure 6, which results in an abrupt shift in the temperatures of the high-temperature and low-temperature streams used for mixing.

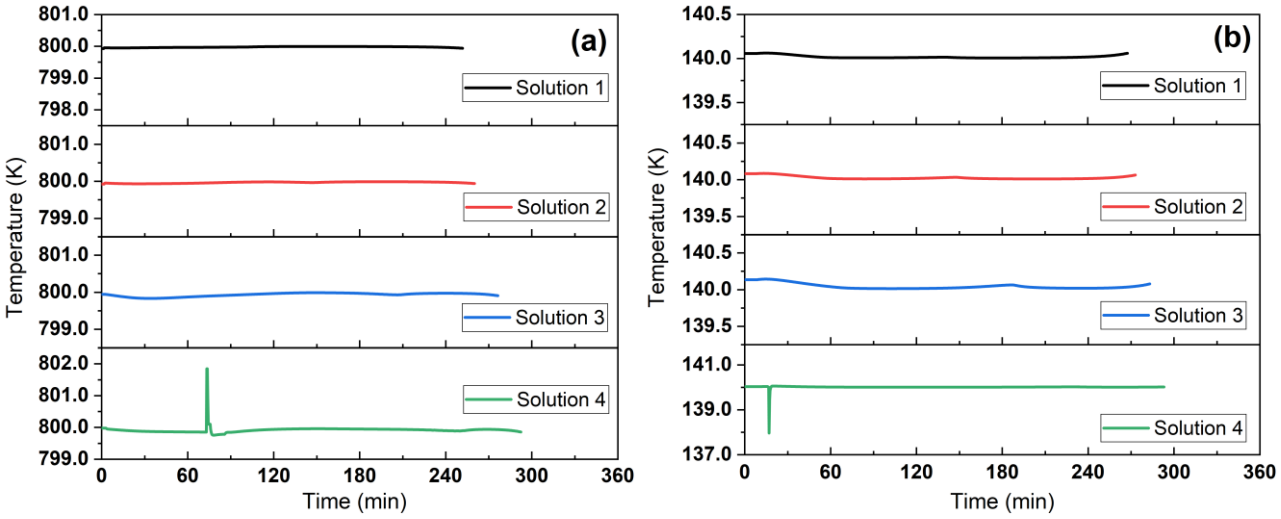


Figure 7. Output temperatures for the four control solutions: (a) CLHS, and (b) CLCS.

The variations in WF mass flow rates within each stage of the CLHS and CLCS are shown in Figure 8. For Solution 1, since the WF is diverted at the Stage 1 outlet, the mass flow rate within Stage 1 remains unchanged. The diverted WF sequentially absorbs hot/cold from Stage 2 to Stage 5, resulting in identical mass flow rates across these stages. This portion of the mass flow rate gradually increases over time until reaching a maximum of 12.5 kg/s. This is because the outlet temperature of each stage gradually decreases within the CLHS and increases within the CLCS, necessitating a greater mass flow to maintain constant temperatures. In Solution 4, the WF mass flow rates within Stages 1 to 3 remain constant, while that in Stage 4 gradually increases. When it reaches the maximum value of 12.5 kg/s, the outlet temperature of Stage 4 in the CLHS drops to 800 K, and that in the CLCS rises to 140 K, indicating that the heating/cooling capacity of Stage 4 has reached its limit. Subsequently, Step 2 is initiated: the mass flow rate in Stages 1 to 4 is maintained at 12.5 kg/s, and the flow in Stage 5 begins to increase gradually from zero.

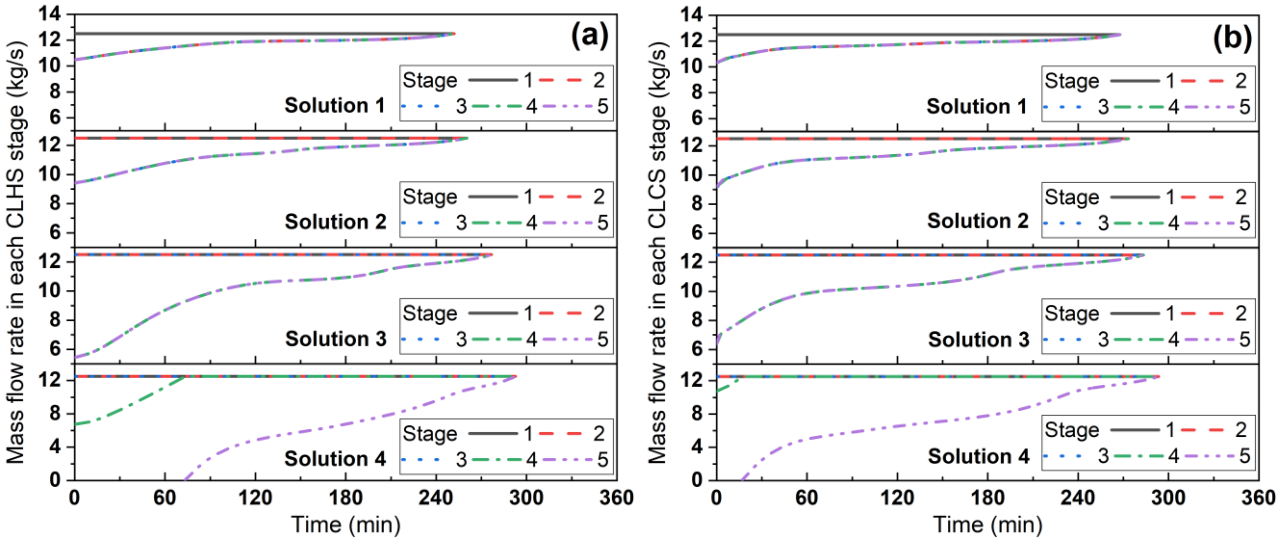


Figure 8. Variations in WF mass flow rates within each stage: (a) CLHS, and (b) CLCS.

It can also be observed that the duration of stable temperature output progressively increases from

Solution 1 to Solution 4, indicating an extended operational duration for the CB system. The stable operating time for Solution 4 is 293 min, which is 41 min longer than for Solution 1. This is attributable to the greater WF mass flow rates within stages 2 and 3 of Solution 4 compared to Solution 1, leading to a more complete utilisation of low-grade hot/cold.

Figure 9 shows the variation of exergy loss rate over time. It can be seen that the exergy loss rates in all solutions fluctuate due to the changes in the WF mass flow rate and temperature. Among the four solutions, Solution 4 exhibits the lowest real-time exergy loss rate. During the discharge process, Solution 4 records the lowest total heat and cold exergy losses, at 40 MJ and 146 MJ, respectively. In contrast, Solution 1 shows the largest, with 401 MJ and 556 MJ. Thus, reduced exergy loss implies greater potential for useful work output, contributing to the longer stable operating duration.

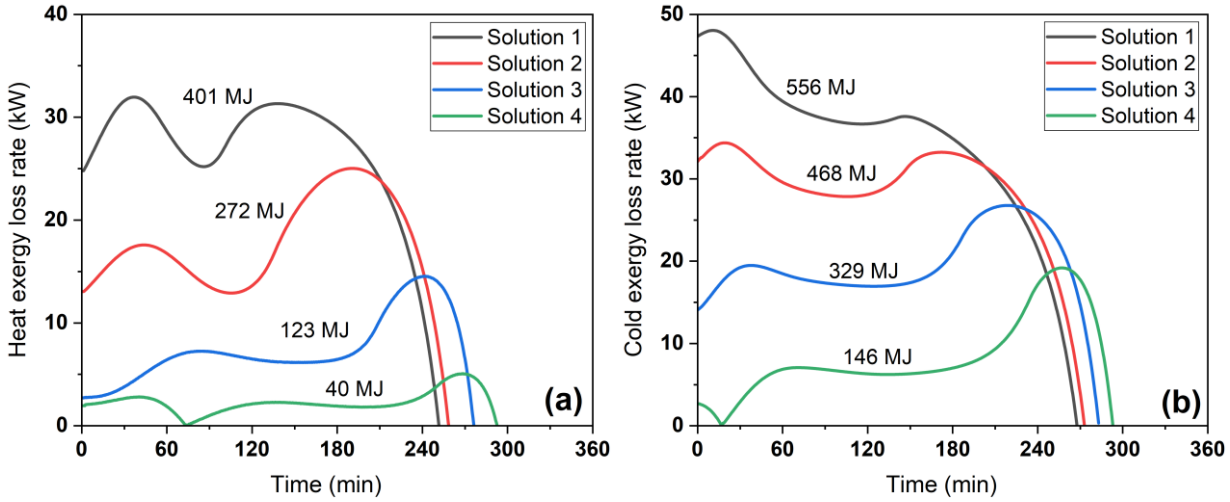


Figure 9. Variation of exergy loss rate over time under the four control solutions.

Figure 10 shows the *RTE* of the CB system in the PES mode for the four control solutions. Solution 4 achieves the highest *RTE* at 48.6%, while Solution 1 yields the lowest *RTE* at 41.8%. This difference arises because, under identical output hot and cold temperature conditions, Solution 4 enables the CLHS and CLCS to deliver heat and cold for a longer duration, thereby extending the system's power generation duration and increasing the total work output. Although various control solutions enable stable operation of the CB system, they result in differing *RTE*s. Solutions exhibiting minimal exergy losses yield higher *RTE*.

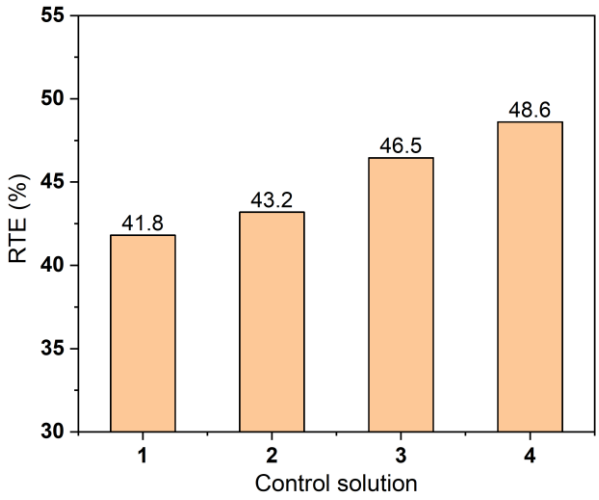


Figure 10. *RTE* of the CB system in PES mode for the four control solutions.

3.1.2 CCHP mode

In the CCHP mode, the CB system is capable of simultaneously generating electricity and supplying single or multiple grades of (hot/cold) thermal energy. While the CLHS and CLCS deliver heat energy at 800 K and cold energy at 140 K to drive the turbine and compressor for power generation, they also provide heat and cold to external demand sectors. Taking the CLHS as an example, a schematic diagram of the internal flow distribution of the WF is shown in Figure 11. The WF stream allocated for heating (indicated by the yellow stream) extracts heat from specific stages based on the thermal storage status of the PCM within each stage, while the flow solution of WF for power generation (indicated by the pink stream) resembles that of the PES mode.

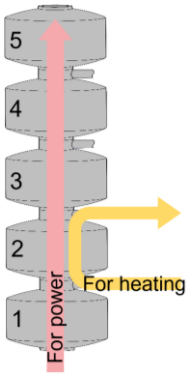


Figure 11. Schematic diagram of WF flow distribution in the CCHP mode.

(1) Single-grade heating/cooling output

While supplying electricity, the system simultaneously delivers heat energy at 600 K and cold energy at 220 K to the user side. Under these demand conditions, Figure 12 shos the temperature profiles of the CB system output. It can be observed that the output temperatures from the CLHS and CLCS remain generally stable and align with the specified requirements, despite minor fluctuations of approximately 2 K. The reasons for the temperature variations in the 800 K heat and 140 K cold used for power generation have been analysed previously in Figure 7. The causes of the fluctuations in the 600 K heat and 220 K cold outputs are further explained in Figure 13.

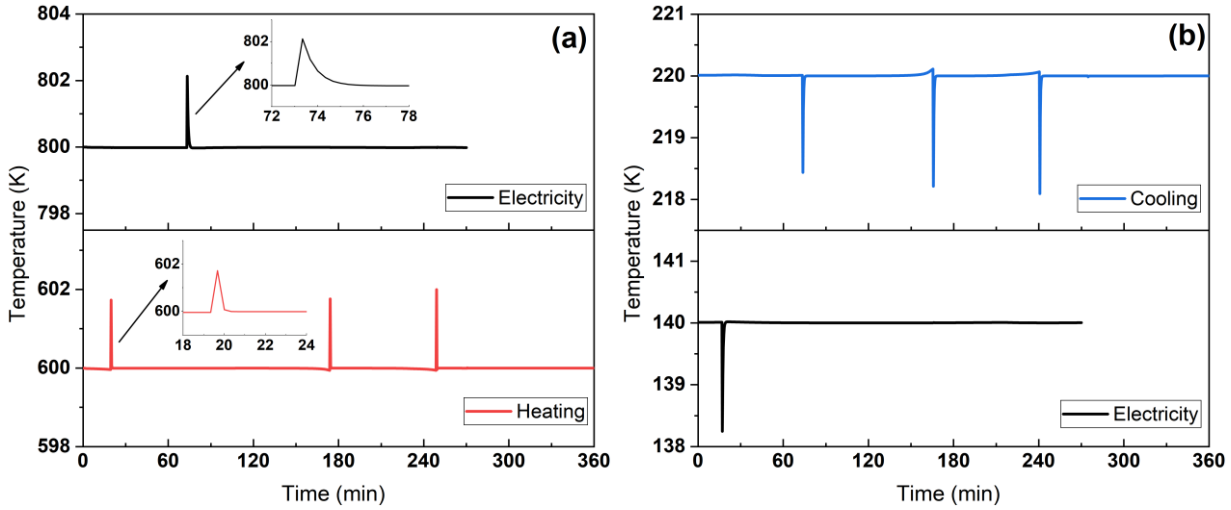


Figure 12. Output temperatures for single-grade heating/cooling supply in CCHP mode: (a) CLHS, and (b) CLCS.

To achieve cascade utilisation of energy and minimise exergy losses, the WF allocated for heating/cooling is first directed into the stage at a lower heat storage temperature (or higher cold storage temperature) to absorb hot/cold. Specifically, the WF initially enters Stage 2. As hot/cold energy is released and becomes insufficient to meet the heating/cooling demand, the WF subsequently enters Stage 3 to continue absorbing the hot/cold energy. This abrupt change in the WF mass flow rate triggers fluctuations in the output temperature of both the CLHS and CLCS, occurring at 20 min and 74 min, respectively. Similarly, when the WF enters Stages 4 and 5 for further heat or cold extraction, each change in the hot/cold energy absorption stage leads to corresponding output temperature fluctuations.

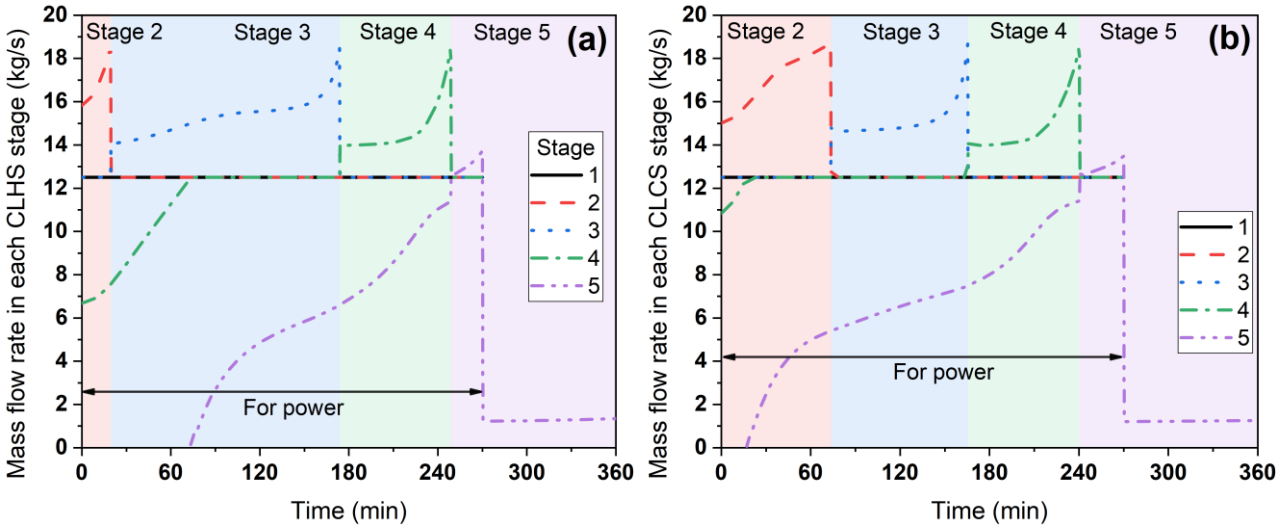


Figure 13. Variation of WF mass flow rate within each stage under single-grade heating/cooling supply in CCHP mode: (a) CLHS, and (b) CLCS.

(2) Multi-grade heating/cooling output

Benefiting from cascade energy storage characteristics, the CB system is also capable of simultaneously supplying multiple grades of thermal energy. For instance, while generating electricity, the system also

delivers 700 K, 600 K, and 500 K heat, as well as 180 K, 220 K, and 260 K cold to the user side. The corresponding actual output temperatures under these conditions are shown in Figure 14. It can be seen that the three grades of heating and cooling outputs from the CLHS and CLCS remain generally stable, though some temperature fluctuations are still present. The electricity generation duration in this scenario is 238 min, representing a reduction of 32 min compared to single-grade heating/cooling output and 55 min relative to the PES mode. This reduction is due to a larger portion of heating and cooling thermal energy being diverted to end-user sectors, thereby diminishing the electrical output capacity.

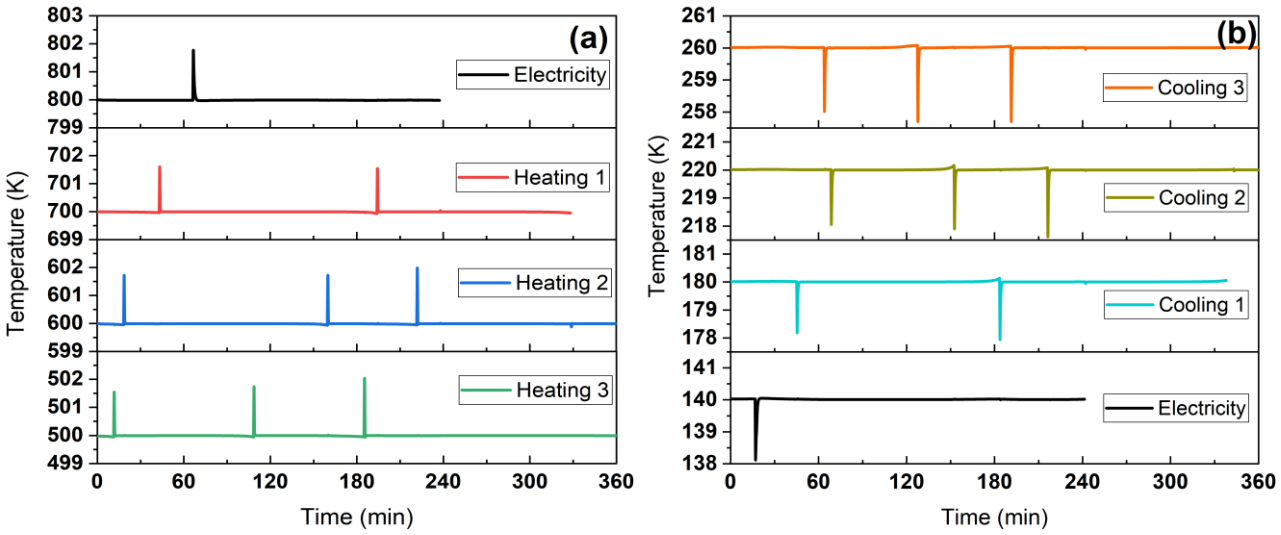


Figure 14. Actual output temperatures under triple-grade heating/cooling supply in CCHP mode: (a) CLHS, and (b) CLCS.

As the CLHS and CLCS simultaneously deliver multiple grades of heat and cold, the variation in flow rates within each stage becomes more complex, as shown in Figure 15. The WF flow rates within the stages of both the CLHS and CLCS exhibit stepwise fluctuations, primarily resulting from changes in the heating/cooling extraction stages (i.e., the stages where WF absorbs hot/cold). Taking Heating 3 (500 K heating output) as an example, the temporal evolution of its extraction stages is shown by the blue curve in Figure 15(c). The WF allocated for heating initially absorbs heat from Stage 1 of the CLHS. At 11 min, as Stage 1 becomes insufficient to meet the heating demand, the WF transitions to Stage 2 until 108 min, then proceeds to Stage 3, and subsequently to Stage 4 at 185 min. Each transition in the active stage causes a fluctuation in the output temperature of Heating 3; however, it does not affect the temperatures of the other heating/cooling outputs. This is because the changes in flow rate only induce negligible fluctuations in the outlet temperatures of the respective stages, and each heating/cooling output is independently regulated by its own controller.

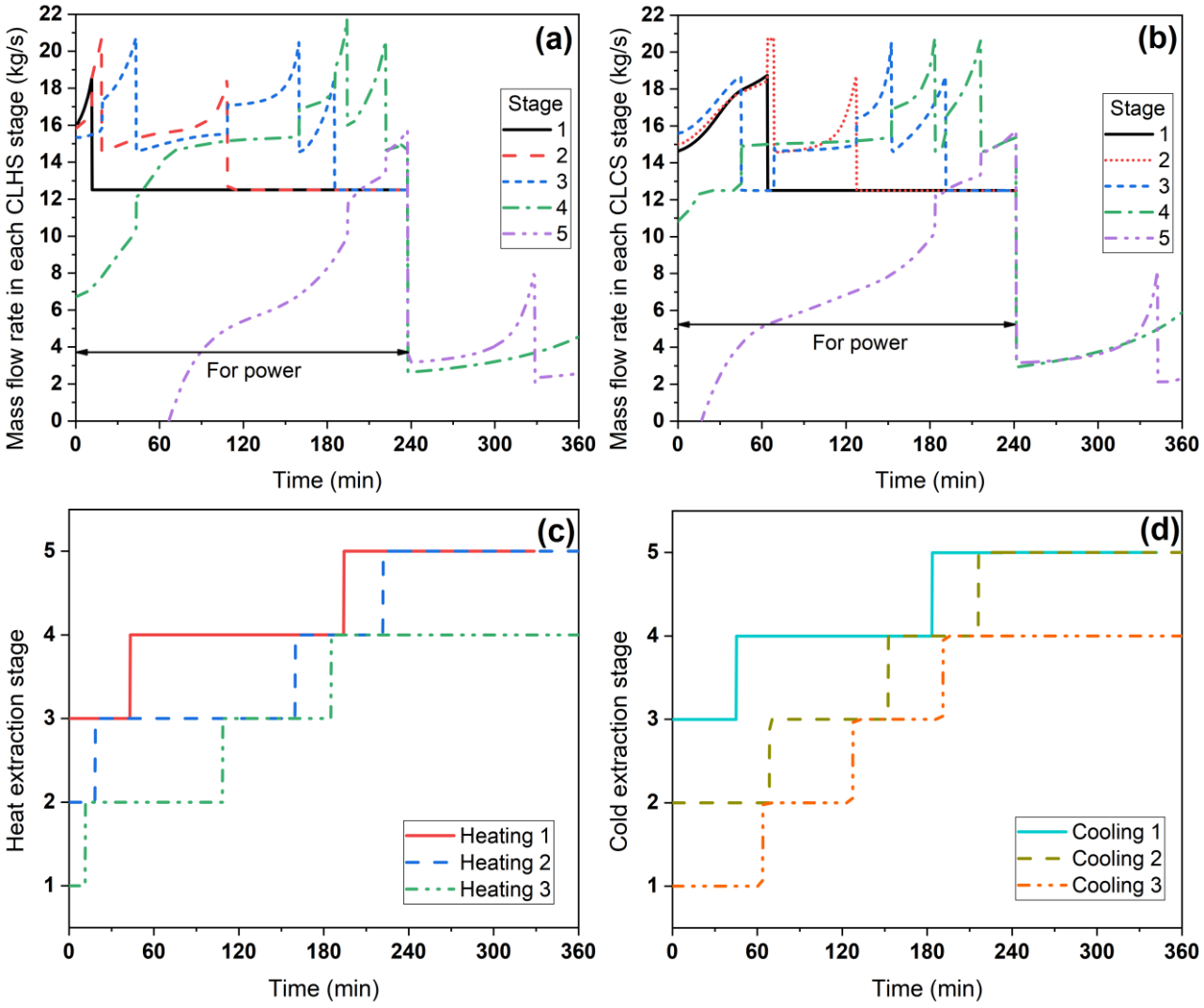


Figure 15. Variation of WF mass flow rate within each stage under simultaneous triple-grade heating/cooling supply in CCHP mode: (a) CLHS, and (b) CLCS.

In addition to the high-grade (hot/cold) thermal energy released by the CLHS and CLCS, the low-grade thermal energy discharged by heat exchangers HX1 and HX2 during the charging and discharging processes can be utilised for district heating and cooling. The performance metrics of the CB system operating in such CCHP mode are shown in Figure 16. The *RTE* in the CCHP mode reaches 39.8%, which is 8.8% lower than that in the PES mode, primarily because portions of the heat and cold within the CLHS and CLCS are directly used for heating and cooling supply. Meanwhile, the *TEE* and *EXE* reach 95.4% and 54.6%, respectively.

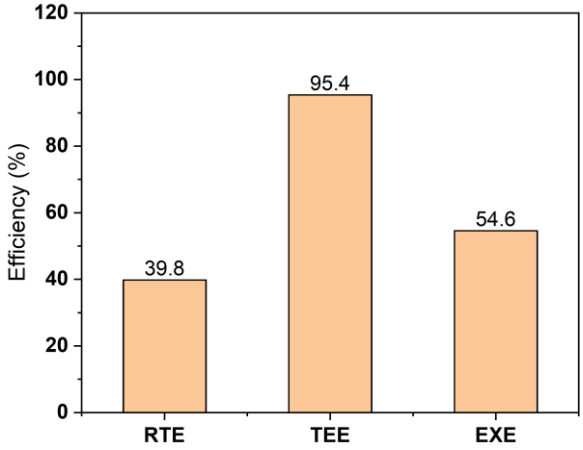


Figure 16. Performance metrics of CB system operating in CCHP mode.

3.2 Variable operating condition

The demands for electricity, heating and cooling on the user side fluctuate over time; thus, it is essential to investigate the system's response characteristics under variable operating conditions and evaluate the performance of the proposed control strategy. This includes examining the fluctuations in electrical, heating and cooling power, as well as the interactions among them.

In CCHP mode, the variation in electrical load is indicated by the black dashed line in Figure 17(a). During 300 s to 350 s, the electrical load decreases to 50% of its design value, ramped down from 1.54 MW to 0.77 MW, and remains steady for a period. During 650 s to 700 s, the load recovers to the design value of 1.54 MW. In tracking the variation of user-side electrical demand, the system’s output power first drops to 0.74 MW and then stabilises at 0.77 MW by 390 s. This demonstrates the system’s capability to adjust to 50% of the design load within 90 s, indicating that the output power effectively tracks the load profile. However, a 4.8% power fluctuation error is observed, attributed to the time delay inherent in the PID controller, which introduces latency in adjusting the WF mass flow rate allocated for power generation. As the WF mass flow rate for power generation varies in response to variations in electrical load, leading to corresponding fluctuations in the outlet temperatures of the CLHS and CLCS. Consequently, the inlet temperatures at both the expander and compressor experience deviations of approximately 5 K, as shown in Figure 17(b) and Figure 17(c).

During variations in electrical load, the heating and cooling power outputs of the system exhibit negligible changes. This stability arises because the mass flow rates of the WF allocated for heating and cooling remain unaffected by electrical load fluctuations. Additionally, both heating and cooling temperatures demonstrate minimal deviation, with maximum temperature variations remaining below 0.1 K. Consequently, fluctuations in thermal and cooling power outputs are less than 0.2%.

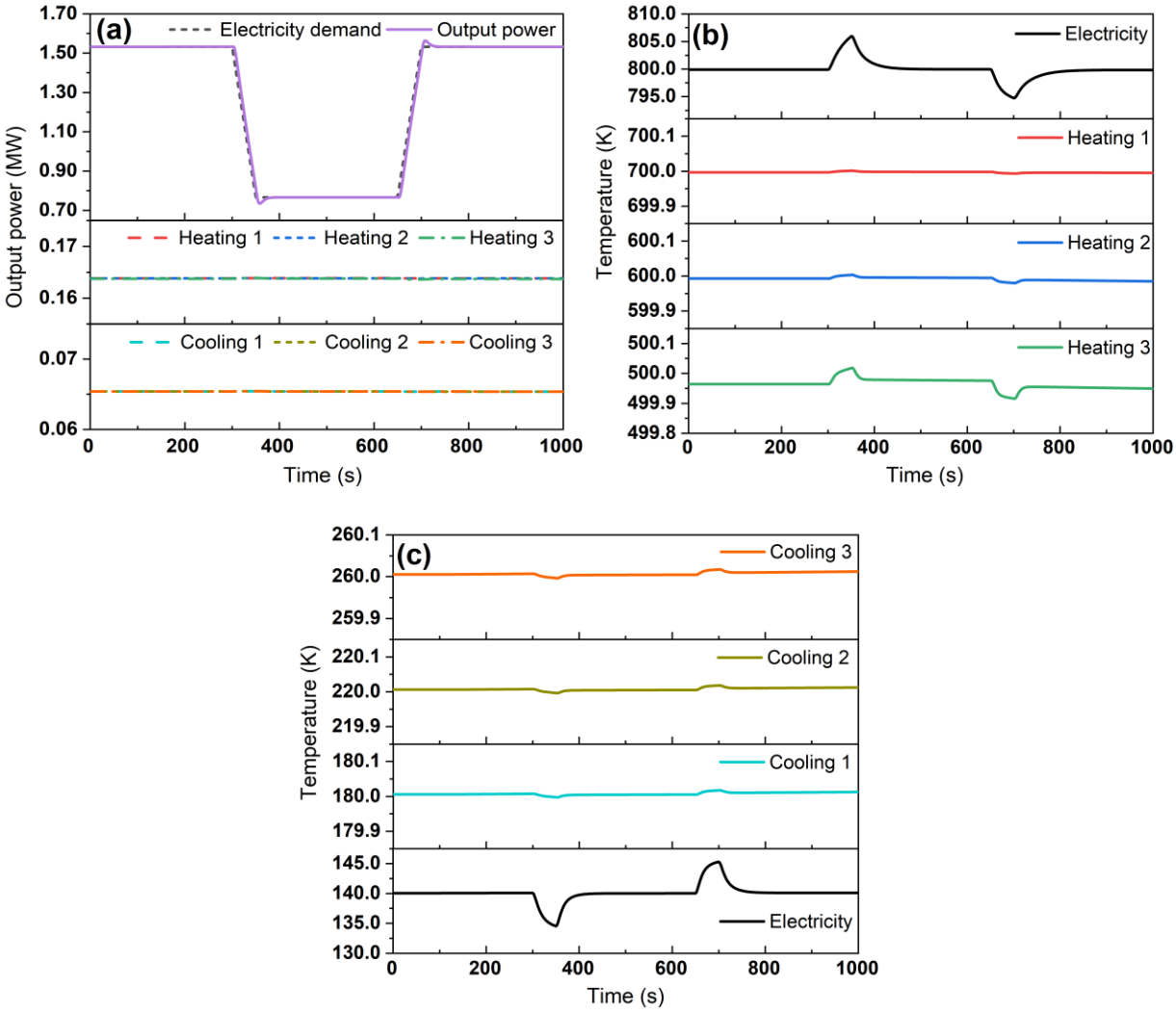


Figure 17. Effects of electrical load variation on system output powers and temperatures: (a) electrical, heating, and cooling output powers, (b) CLHS output temperatures, and (c) CLCS output temperatures.

The heating power demand variation are shown by the black line in Figure 18(a). At 300 s, the heating demands simultaneously double to 0.32 MW across all three heating levels, before returning to their initial value (0.16 MW) at 700 s. It can be observed that, in tracking the user-side heating demand, the system's heating power outputs first rise to 0.29 MW and then gradually increase to the target value of 0.32 MW within 200 s. This delayed response is due to the instantaneous increase in the WF mass flow rate for heating, which leads to a transient reduction in the CLHS outlet temperature, as shown in Figure 18(b). At 300 s, all heating temperatures decrease by 6 K, causing the heating power to temporarily fail to track the load promptly. Similarly, at 700 s, the heating power outputs initially drop to 0.19 MW and then gradually decrease to the target value of 0.16 MW over the next 200 s.

During heating load fluctuations, the cooling and electrical power outputs of the system exhibit negligible changes, as the mass flow rates of the WF allocated for power generation and cooling are unaffected by variations in heating load. However, due to changes in the total WF mass flow rate within the CLHS, the temperature at the expander inlet (utilised for power generation) experiences slight fluctuations of approximately 0.2 K, resulting in a minor electrical power deviation of about 0.02%.

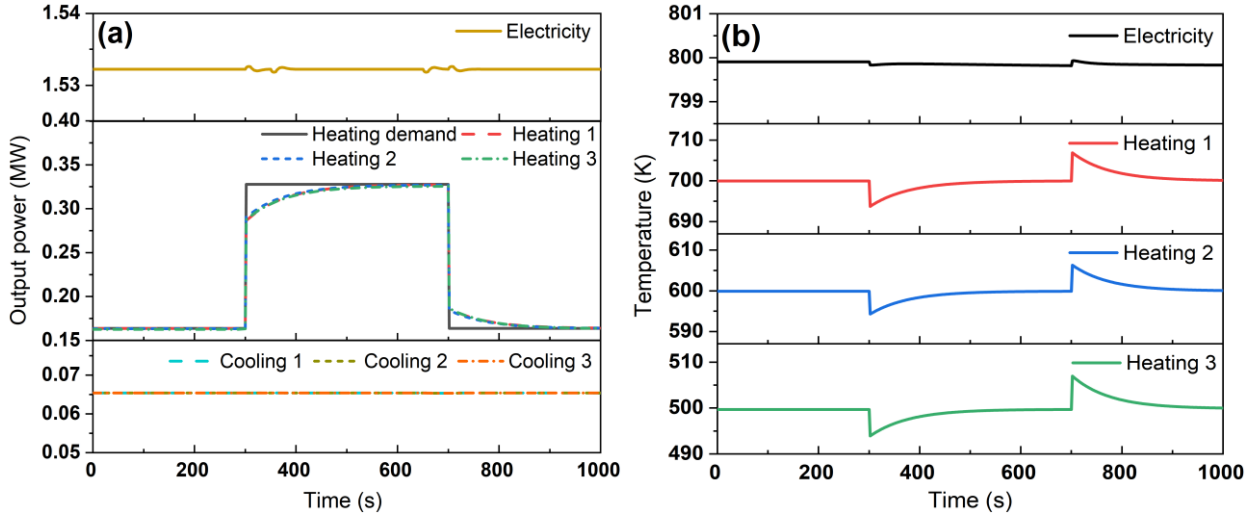


Figure 18. Effects of heating load variation on system output powers and temperatures: (a) electrical, heating, and cooling output powers, and (b) CLHS output temperatures.

The variations in cooling power demands are shown by the black line in Figure 19(a). At 300 s, the cooling power demands simultaneously double to 0.13 MW across all three cooling levels before recovering to their initial value of 0.07 MW at 700 s. As shown, during the process of tracking the fluctuating user-side cooling demand, the cooling power outputs first rise to 0.09 MW, and subsequently increase gradually to the set value of 0.13 MW within 200 s. This response mirrors that of the heating power response: a sudden increase in the mass flow rate of the WF allocated for cooling induces an instantaneous rise in the CLCS outlet temperature, as shown in Figure **19**(b). At 300 s, all cooling temperatures increase by 6 K, which delays the target load from being reached.

During cooling load fluctuations, the electrical and heating power outputs exhibit negligible changes. This stability arises because the WF flow allocated for power generation and heating remain unaffected by variations in the cooling load. Although a slight fluctuation occurs in the temperature at the compressor inlet (used for power generation), it is insufficient to induce any significant change in the electrical power output.

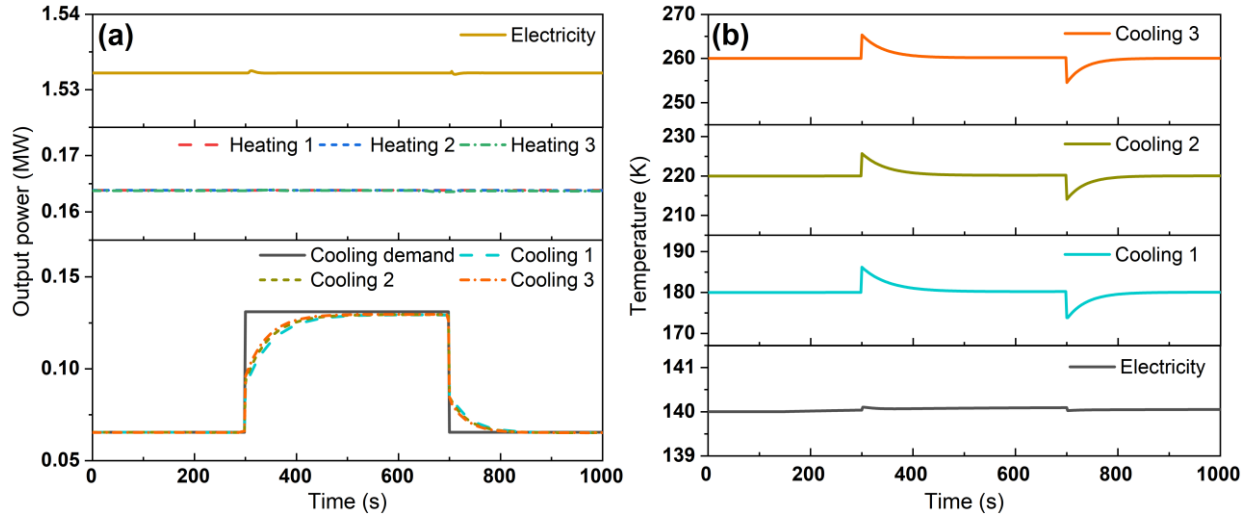


Figure 19. Effects of cooling load variation on system output powers and temperatures: (a) electrical, heating, and cooling output powers, and (b) CLCS output temperatures.

The response fluctuation error in the system's output power response is influenced by the magnitude of load variations. A smaller error indicates superior load-following capability. Figure 20 shows the fluctuation error in output power when the system shifts from the design load to various loads. It is observed that when the electrical load decreases to 50% of the design value, the output power fluctuation error remains as low as 4%. In contrast, when the electrical load decreases to 10% of the design value, the error increases significantly to 36%. This demonstrates that the system's electrical load-tracking performance deteriorates substantially under excessively low-load conditions.

Figure 20(b) and Figure 20(c) show the fluctuation errors in heating and cooling power outputs under different loads. It is evident that the fluctuation errors of both heating and cooling power increase with greater deviation from the design load. When the loads decrease to 20% of the design value, the fluctuation errors in heating and cooling power reach 13% and 54%, respectively. Conversely, when the loads increase to 200% of the design value, the corresponding errors are -12% and -30%, respectively.

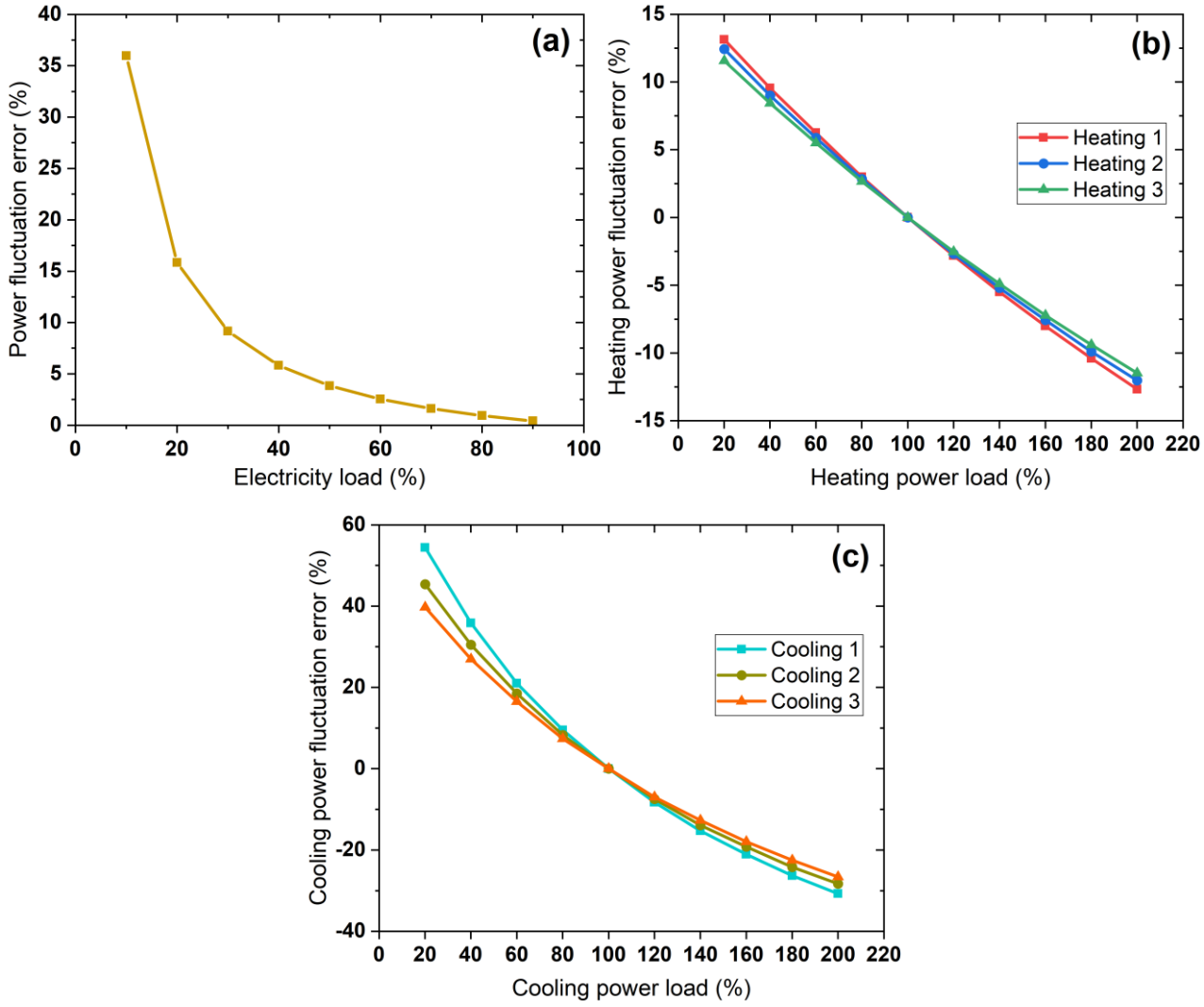


Figure 20. Effect of load levels on power fluctuation errors: (a) electrical, (b) heating, and (c) cooling.

Finally, it is noted that the fluctuation errors differ across heating/cooling grades, with high-grade energy outputs (e.g., Heating 1/Cooling 1) demonstrating more pronounced deviations. For instance, at 20% of the

design load, the fluctuation error of Cooling 1 is 54%, exceeding that of Cooling 2 (45%) and Cooling 3 (40%). This is because Cooling 1 extracts cold from Stage 3 of the CLCS, Cooling 2 from Stage 2, and Cooling 3 from Stage 1. The WF sequentially flows through the Stage 1, Stage 2 and Stage 3 of the CLCS. Temperature fluctuations generated in upstream stages propagate downstream, leading to cumulative error amplification. As Cooling 1 resides at the most downstream position in the CLCS, it exhibits the largest fluctuation error.

4. Conclusions

In this paper, a dynamic simulation model of a CB-based CCHP system incorporating CLHCS is established, and a novel temperature-adaptive control strategy is developed to enable rapid and flexible delivery of electricity alongside multi-grade thermal energy for both heating and cooling.

Under design conditions, the proposed temperature-adaptive control strategy enables the CLHS and CLCS to stably supply single or multiple temperature grades of heating/cooling, ensuring stable operation of the CB system. The control solution minimising exergy loss achieves optimal performance, with the longest power generation duration of 293 min and the highest *RTE* of 49%.

When the system simultaneously delivers electricity and multi-grade hot/cold energy, stage switching within the CLHS/CLCS induces manageable output temperature fluctuations of approximately 2 K. In CCHP mode, the system demonstrates impressive energy utilisation efficiency, achieving a *TEE* of 95% and an *EXE* of 55%.

The control strategy also demonstrates feasibility under variable operating conditions. For a 3 MW CB-based CCHP system, the electrical, heating, and cooling power outputs can all effectively track user-side load variations within 200 s. Furthermore, The CB-based CCHP system exhibits robust synergistic anti-disturbance capability: disturbances in any single power output (electrical, heating or cooling) are effectively contained within the affected output. This decoupling characteristic prevents significant propagation or instability in the other power outputs, thereby ensuring robust and reliable system operation in complex multi-energy supply scenarios and significantly mitigating the risk of cascading instability induced by fluctuations in a single load.

The power output response fluctuation errors increase with the deviation of the load from the design value. When the load decreases to 50% of its design value, the fluctuation errors for electrical, heating, and cooling power outputs are 4%, 8%, and 22%, respectively. Moreover, during simultaneous multi-grade heating/cooling delivery, higher-grade heating/cooling powers exhibit more pronounced fluctuation errors compared to lower-grade powers.

Overall, this work fills critical gaps by clarifying the dynamic behaviour of CB-based CCHP systems with CLHCSs and by introducing a novel control strategy that unites high responsiveness, stability and multi-energy coordination. These findings offer a technical foundation for the practical deployment of such systems, supporting deep decarbonisation of the energy sector and enabling intelligent, demand-responsive energy management.

Acknowledgements

This work was supported by the National Natural Science Foundation of China (Grant No. 51906150), the Future Foundation of Energy Science (Grant No. WLNY-MS-2022-010). The work was also supported by the UK Engineering and Physical Sciences Research Council (EPSRC) [grant number EP/S032622/1]. Data

supporting this publication can be obtained on request from thameswalker@outlook.com and cep-lab@imperial.ac.uk. For the purpose of Open Access, the authors have applied a CC BY public copyright licence to any Author Accepted Manuscript version arising from this submission.

References

[1] IRENA. Renewable energy statistics 2024. Abu Dhabi: International Renewable Energy Agency; 2024.

[2] Wang YJ, Wang R, Tanaka K, Ciais P, Penuelas J, Balkanski Y, et al. Accelerating the energy transition towards photovoltaic and wind in China. Nature. 2023;619:761–7.

[3] Saher S, Johnston S, Esther-Kelvin R, Pringle JM, MacFarlane DR, Matuszek K. Trimodal thermal energy storage material for renewable energy applications. Nature. 2024;636:622-6.

[4] Cao RF, Li WQ, Ni HX, Kuang CX, Liang YT, Fu ZH. Comprehensive assessment and optimization of a hybrid cogeneration system based on compressed air energy storage with high-temperature thermal energy storage. Frontiers in Energy. 2025;19:175-92.

[5] Li YH, Xu WB, Zhang M, Zhang CL, Yang T, Ding HY, et al. Performance analysis of a novel medium temperature compressed air energy storage system based on inverter-driven compressor pressure regulation. Frontiers in Energy. 2025;19:144-56.

[6] Rehman S, Al-Hadhrami LM, Alam MM. Pumped hydro energy storage system: A technological review. Renewable and Sustainable Energy Reviews. 2015;44:586-98.

[7] Galos J, Pattarakunnan K, Best AS, Kyratzis IL, Wang CH, Mouritz AP. Energy storage structural composites with integrated lithium-ion batteries: A review. Advanced Materials Technologies. 2021;6:2001059.

[8] Olympios AV, McTigue JD, Farres-Antunez P, Tafone A, Romagnoli A, Li YL, et al. Progress and prospects of thermo-mechanical energy storage-a critical review. Progress in Energy. 2021;3:022001.

[9] Zhao Y, Li MJ, Wang K, Sciacovelli A, Qin CS, Lecompte S, et al. Thermo-mechanical energy storage technologies: Innovations, challenges and future directions. Frontiers in Energy. 2025;19:115-6.

[10] Georgiou S, Aunedi M, Strbac G, Markides CN. On the value of liquid-air and pumped-thermal electricity storage systems in low-carbon electricity systems. Energy. 2020;193:116680.

[11] White A, Parks G, Markides CN. Thermodynamic analysis of pumped thermal electricity storage. Applied Thermal Engineering. 2013;53:291-8.

[12] Liang T, Vecchi A, Knobloch K, Sciacovelli A, Engelbrecht K, Li Y, et al. Key components for Carnot Battery: Technology review, technical barriers and selection criteria. Renewable and Sustainable Energy Reviews. 2022;163:112478.

[13] Huang J, Zhao Y, Song J, Huang S, Wang K, Rao Z, et al. A review of progress in thermo-mechanical energy storage technologies for combined cooling, heating and power applications. Frontiers in Energy. 2025;19:117-43.

[14] Yang H, Li JD, Ge ZH, Yang LJ, Du XZ. Dynamic characteristics and control strategy of pumped thermal electricity storage with reversible Brayton cycle. Renewable Energy. 2022;198:1341-53.

[15] Yang H, Li J, Ge Z, Yang L, Du X. Dynamic performance for discharging process of pumped thermal electricity storage with reversible Brayton cycle. Energy. 2023;263:125930.

[16] Frate GF, Pettinari M, Di Pino Incognito E, Costanzi R, Ferrari L. Dynamic Modelling of a Brayton PTES System. ASME Turbo Expo 2022: Turbomachinery Technical Conference and Exposition2022.

[17] Lu C, Shi X, He Q, Liu Y, An X, Cui S, et al. Dynamic modeling and numerical investigation of novel pumped thermal electricity storage system during startup process. Journal of Energy Storage. 2022;55:105409.

[18] Shi X, He Q, Lu C, Wang T, Cui S, Du D. Variable load modes and operation characteristics of closed Brayton cycle pumped thermal electricity storage system with liquid-phase storage. Renewable Energy. 2023;203:715-30.

[19] An XG, He Q, Zhang QX, Liu RA, Lu C, Du DM. Physical modeling and dynamic characteristics of pumped

thermal energy storage system. Energy. 2024;290:130144.
[20] McTigue J, Neises T. Off-design operation and performance of pumped thermal energy storage. Journal of Energy Storage. 2024;99:113355.
[21] Frate GF, Paternostro L, Ferrari L, Desideri U. Off-Design of a Pumped Thermal Energy Storage Based on Closed Brayton Cycles. Journal of Engineering for Gas Turbines and Power. 2022;144.
[22] Cascetta M, Licheri F, Merchán RP, Petrollese M. Operating performance of a Joule-Brayton pumped thermal energy storage system integrated with a concentrated solar power plant. Journal of Energy Storage. 2023;73:108865.
[23] Canpolat Tosun D, Açıkkalp E, Altuntas O, Hepbasli A, Palmero-Marrero AI, Borge-Diez D. Dynamic performance and sustainability assessment of a PV driven Carnot battery. Energy. 2023;278:127769.
[24] Wang P, Li Q, Wang S, He C, Wu C. Off-design performance evaluation of thermally integrated pumped thermal electricity storage systems with solar energy. Energy Conversion and Management. 2024;301:118001.
[25] Huang J, Zhao Y, Song J, Wang K, Zhu P, Liu B, et al. Thermodynamic investigation of a Joule-Brayton cycle Carnot battery multi-energy system integrated with external thermal (heat and cold) sources. Applied Energy. 2025;377:124652.
[26] Zhao Y, Huang JX, Song J, Ding YL. Thermodynamic investigation of a Carnot battery based multi-energy system with cascaded latent thermal (heat and cold) energy stores. Energy. 2024;296:131148.
[27] Zhao Y, Song J, Zhao CY, Zhao YL, Markides CN. Thermodynamic investigation of latent-heat stores for pumped-thermal energy storage. Journal of Energy Storage. 2022;55:105802.
[28] Zhao Y, Xie Y, Song J, Wang K, Cui L, Zhang H. Second-law thermodynamic assessment of cascaded latent-heat stores for pumped-thermal electricity storage. Applied Thermal Engineering. 2025;262:125290.
[29] Zhao Y, You Y, Liu HB, Zhao CY, Xu ZG. Experimental study on the thermodynamic performance of cascaded latent heat storage in the heat charging process. Energy. 2018;157:690-706.
[30] Zhang N, Cai RX. Analytical solutions and typical characteristics of part-load performances of single shaft gas turbine and its cogeneration. Energy Conversion and Management. 2002;43:1323-37.
[31] Zhang H, Wang L, Lin XP, Chen HS. Combined cooling, heating, and power generation performance of pumped thermal electricity storage system based on Brayton cycle. Applied Energy. 2020;278:115607.
[32] Fang M, Chen GM. Effects of different multiple PCMs on the performance of a latent thermal energy storage system. Applied Thermal Engineering. 2007;27:994-1000.
[33] Li M-J, Li M-J, Xue X-D, Li D. Optimization and design criterion of the shell-and-tube thermal energy storage with cascaded PCMs under the constraint of outlet threshold temperature. Renewable Energy. 2022;181:1371-85.
[34] Mostafavi Tehrani SS, Shoraka Y, Nithyanandam K, Taylor RA. Cyclic performance of cascaded and multi-layered solid-PCM shell-and-tube thermal energy storage systems: A case study of the 19.9 MWe Gemasolar CSP plant. Applied Energy. 2018;228:240-53.
[35] Shah RK, Sekulic DP. Fundamentals of heat exchanger design: John Wiley & Sons; 2003.
[36] Bergman TL, Incropera FP, DeWitt DP, Lavine AS. Fundamentals of heat and mass transfer. 7th ed. New Jersey: John Wiley & Sons; 2011.
[37] Deng T, Li X, Wang Q, Ma T. Dynamic modelling and transient characteristics of supercritical CO2 recompression Brayton cycle. Energy. 2019;180:292-302.
[38] Lacroix M. Numerical-simulation of a shell-and-tube latent-heat thermal-energy storage unit. Solar Energy. 1993;50:357-67.
[39] Pra F, Tochon P, Mauget C, Fokkens J, Willemsen S. Promising designs of compact heat exchangers for modular HTRs using the Brayton cycle. Nuclear Engineering and Design. 2008;238:3160-73.
[40] Yang H, Li J, Ge Z, Yang L, Du X. Dynamic characteristics and control strategy of pumped thermal electricity storage with reversible Brayton cycle. Renewable Energy. 2022;198:1341-53.
[41] Sciacovelli A, Li Y, Chen H, Wu Y, Wang J, Garvey S, et al. Dynamic simulation of Adiabatic Compressed Air

Energy Storage (A-CAES) plant with integrated thermal storage – Link between components performance and plant performance. Applied Energy. 2017;185:16-28.
[42] Zhang H, Wang L, Lin X, Chen H. Combined cooling, heating, and power generation performance of pumped thermal electricity storage system based on Brayton cycle. Applied Energy. 2020;278.
[43] McTigue JD, White AJ, Markides CN. Parametric studies and optimisation of pumped thermal electricity storage. Applied Energy. 2015;137:800-11.
[44] Wang L, Lin XP, Chai L, Peng L, Yu O, Chen HS. Cyclic transient behavior of the Joule-Brayton based pumped heat electricity storage: Modeling and analysis. Renewable & Sustainable Energy Reviews. 2019;111:523-34.
[45] Zhao YL, Song J, Liu M, Zhao Y, Olympios AV, Sapin P, et al. Thermo-economic assessments of pumped-thermal electricity storage systems employing sensible heat storage materials. Renewable Energy. 2022;186:431-56.
[46] Tehrani SSM, Taylor RA, Saberi P, Diarce G. Design and feasibility of high temperature shell and tube latent heat thermal energy storage system for solar thermal power plants. Renewable Energy. 2016;96:120-36.
[47] Zhao Y, Zhao CY, Markides CN, Wang H, Li W. Medium- and high-temperature latent and thermochemical heat storage using metals and metallic compounds as heat storage media: A technical review. Applied Energy. 2020;280:115950.
[48] Mohamed SA, Al-Sulaiman FA, Ibrahim NI, Zahir MH, Al-Ahmed A, Saidur R, et al. A review on current status and challenges of inorganic phase change materials for thermal energy storage systems. Renewable & Sustainable Energy Reviews. 2017;70:1072-89.
[49] Yang LZ, Villalobos U, Akhmetov B, Gil A, Khor JO, Palacios A, et al. A comprehensive review on sub-zero temperature cold thermal energy storage materials, technologies, and applications: State of the art and recent developments. Applied Energy. 2021;288:116555.